LAWRENCE
LIVERMORE
NATIONAL
LABORATORY

UCRL-CONF-221590

Characterizing Electron Temperature Gradient Turbulence Via Numerical Simulation

W. M. Nevins, J. Candy, S. Cowley, T. Dannert, A. Dimits, W. Dorland, C. Estrada-Mila, G. W. Hammett, F. Jenko, M. J. Pueschel, D. E. Shumaker

May 23, 2006

PSACI PAC
Princeton, NJ, United States
May 29, 2006 through June 1, 2006

Disclaimer

Characterizing

electron temperature gradient turbulence

via numerical simulation

W.M. Nevins,[a] J. Candy,[b] S. Cowley,[c]

T. Dannert,[d] A. Dimits,[a] W. Dorland,[e]

C. Estrada-Mila,[f] G.W. Hammett,[g] F. Jenko,[h]

M.J. Pueschel,[h] and D.E. Shumaker[a]

[a]Lawrence Livermore National Laboratory, Livermore, CA 94551

[b]General Atomics, San Diego, CA 92186

[c]Department of Physics and Astronomy, UCLA, Los Angeles, CA 90095-1547

[d]Centre de Recherches en Physique des Plasmas (CRPP), Ecole Polytechnique Federale de Lausanne (EPFL), CH-1015 Lausanne, Switzerland

[e]University of Maryland, College Park, MD 20742

[f] Department of Mechanical and Aerospace Engineering, UCSD, San Diego, CA 92093

[g] Princeton Plasma Physics Laboratory, Princeton, NJ 08536

[h]Max-Planck Institut für Plasmaphysik, D-85748 Garching, Germany

Abstract

Numerical simulations of electron temperature gradient (ETG) turbulence are presented which characterize the ETG fluctuation spectrum, establish limits to the validity of the adiabatic ion model often employed in studying ETG turbulence, and support the tentative conclusion that plasma-operating regimes exist in which ETG turbulence produces sufficient electron heat transport to be experimentally relevant. We resolve prior controversies regarding simulation techniques and convergence by benchmarking simulations of ETG turbulence from four microturbulence codes, demonstrating agreement on the electron heat flux, correlation functions, fluctuation intensity, and *rms* flow shear at fixed simulation cross section and resolution in the plane perpendicular to the magnetic field. Excellent convergence of both continuum and particle-in-cell codes with time step and velocity-space resolution is demonstrated, while numerical issues relating to perpendicular (to the magnetic field) simulation dimensions and resolution are discussed. A parameter scan in the magnetic shear, s, demonstrates that the adiabatic ion model is valid at small values of s ($s<0.4$ for the parameters used in this scan) but breaks down at higher magnetic shear. A proper treatment employing gyro-kinetic ions reveals a steady increase in the electron heat transport with increasing magnetic shear, reaching electron heat transport rates consistent with analyses of experimental tokamak discharges.

I. Introduction

We present direct numerical simulations of electron temperature gradient (ETG) turbulence that serve to characterize the ETG fluctuation spectrum, establish limits to the validity of the adiabatic ion model often employed in studying ETG turbulence, and support the tentative conclusion that plasma operating regimes exist in which ETG turbulence can produce sufficient electron heat transport to be experimentally relevant. In the electrostatic approximation the equations describing ETG modes[1-4] are nearly isomorphic to those describing ion temperature gradient (ITG) modes when considering ETG turbulence for which $k_\perp \rho_i >> 1$ (where $k_\perp$ is the component of the ETG wavenumber perpendicular to the magnetic field and ρ_i is the ion gyroradius) so that the ion response is adiabatic and $k\lambda_{De} << 1$ (where λ_{De} is the electron Debye length) so that space charge effects can be ignored. This near isomorphism between ITG and ETG turbulence involves exchanging ion scales (ρ_i and the ion thermal velocity, v_{ti}) for the corresponding electron scales (the electron gyroradius, ρ_e and the electron thermal velocity, v_{te}). As a result the transport associated with ETG turbulence is measured in electron gyro-Bohms, which, for deuterium plasmas, are 60 times smaller than the ion gyro-Bohms used to calibrate ITG turbulence.

The definition of a gyro-Bohm involves a macroscopic length, taken to be the temperature gradient scale length, L_T, throughout this paper. Hence, $\chi_{GB} \equiv (\rho/L_T)\rho v_{th}$. The

ion thermal conductivity observed in numerical simulations of ITG turbulence rarely exceeds two ion gyro-Bohms[5-9] and there has been substantial controversy regarding how strong ETG turbulence is and whether it can produce sufficiently large electron thermal transport to be experimentally relevant. Some workers[10-12] have reported relatively low levels of electron thermal transport, while others[13-20] report electron thermal conductivities from microturbulence simulations exceeding ten electron gyro-Bohms. However, all of these previous simulations found significant enhancement of $\chi_e/\chi_{e,GB}$ for ETG relative to the value of $\chi_i/\chi_{i,GB}$ seen in equivalent ITG simulations (the reported value of $\chi_e = 3.2\ \chi_{e,GB}$ in Refs. 11-12 is enhanced by a factor of ~4 over the equivalent adiabatic-electron ITG results in Ref.8). We will show than even an electron thermal conductivity of a few electron gyro-Bohms is sufficient to explain the electron transport in some tokamak discharges.

Some of the differences between ETG simulation results can be explained by differences in the operating point of the background plasma supporting the ETG turbulence. However, many of these simulations[11-21] employed similar operating points — an electron analogue of the Cyclone project's ITG benchmark described in Ref. 8 (but note that Refs. 13-15 excluded trapped electrons by setting the local inverse aspect ratio to zero). Nevins *et al.*[21] demonstrated that the low level of electron thermal transport (3 electron gyro-Bohms) at this operating point reported in Refs. 11 and 12 resulted from excessive discrete particle noise in these particle-in-cell (PIC) simulations of ETG turbulence. To study these issues further, verify that independent simulations can achieve consistent ETG results at the same operating point and numerical resolution, and at the

request of the Plasma Science and Advanced Computing Initiative program advisory committee,[22] we undertook the benchmarking ETG benchmarking effort reported in Secs. II thru IV following.

The work of Nevins *et al.*[21] and initial efforts by this group demonstrated that the ETG turbulence observed in simulations at the electron analogue of the Cyclone ITG benchmark point[8] including trapped particles is so violent as to make PIC simulations impractical, while continuum simulations at this operating point are limited by the (nonlinear) Courant condition for the $E\times B$ flow (forcing codes with adaptive integrators to progressively shorter time steps) and often fail to reach a steady-state. (The simulations of Refs. 13-15 had trapped particles turned off. This provided a long-wavelength cut off that helped achieve saturation.) Hence, we have concluded that the electron analogue of the Cyclone ITG benchmark point is not an appropriate operating point for benchmarking simulations of ETG turbulence. We present an alternate ETG benchmark operating point in Sec. II together with linear analysis of ETG instability at this operating point. Convergence tests at this new benchmark point are presented in Sec. III, where we demonstrate excellent convergence in time step and velocity space resolution and investigate issues relating to numerical convergence with respect to the perpendicular (to the magnetic field, $\boldsymbol{B}$) size and resolution of the simulation. Simulation results from the continuum gyrokinetic codes GYRO,[23] GS2,[14] and GENE[13] as well as the PIC gyrokinetic code PG3EQ[7] are compared in Sec. IV. In Sec. V we present results from a parameter scan in which the electron heat transport due to ETG turbulence

increases from about 3 electron gyro-Bohms to 14 electron gyro-Bohms as the magnetic shear is varied from 0.1 to 0.8. In Sec. VI we revisit selected analyses of electron heat transport in tokamak discharges, concluding that an electron thermal conductivity between 5 and 10 electron gyro-Bohms is sufficient to explain the electron heat transport in many tokamak discharges. These results are discussed further in Sec. VII.

II. The Benchmark Operating Point

The establishment of a common benchmark is an important step in computational studies of a new regime of plasma microturbulence. This benchmark serves as a means of verifying that different plasma microturbulence simulations codes obtain substantially the same transport and turbulent fluctuation characteristics at a common operating point. The demonstration that a particular plasma microturbulence code can reproduce the benchmark results becomes an important verification exercise for that code. It provides an anchor for future parameter scans, serves to enhance community confidence in the simulation results, and largely eliminates numerical issues when comparing simulation results between codes at different operating points, thereby shifting the focus of discussions from the accuracy of particular simulation codes to the underlying physics issues.

Such a common benchmark was established for ITG turbulence by the Cyclone project.[8] This effort largely eliminated controversy between practitioners using continuum and particle-in-cell techniques over turbulence simulation results in the ITG regime, and provided a basis for understanding the size scaling of ITG turbulence[24] observed in global simulations.[25,26] Differences between gyrofluid and gyrokinetic simulation results at this benchmark point served to focus attention on the importance of zonal flows generated by ITG turbulence and motivated further development of the theory of zonal flow generation.[27-29]

The numerical models employed in the benchmarking exercise described in this paper differ from those employed for the kinetic simulations of ITG turbulence in Ref. 8 in that the kinetic species is understood to be electrons (rather than ions as in Ref. 8) and the density of the adiabatic species entering the gyrokinetic Poisson equation is proportional to the full potential, ϕ, rather than to the difference between the local potential and its flux surface average, $\phi - \langle\phi\rangle$, as in ITG turbulence simulations. This difference arises because the ions are assumed to have gyro orbits large compared to the perpendicular (to $\boldsymbol{B}$) scale of both the ETG modes and any zonal or geodesics acoustic modes generated by the ETG turbulence. We note that previous work[13,30] shows that finite-ion-orbit effects can be important to the development of the long wavelength end of the ETG turbulent spectrum, and consider this effect in Sec. V below.

Previous workers[11,12,19-21,31] have focused on an electron analogue of the operating point chosen for the Cyclone ion temperature gradient benchmark exercise.[8] This operating point has not produced a successful ETG benchmark. The basic problem is that ETG turbulence is too violent at this operating point, yielding poor performance from all codes. Jenko and Dorland[13-15] solved this problem in their pioneering work on ETG turbulence simulation by removing the trapped electrons. They accomplished this by reducing the local aspect ratio from the Cyclone benchmark value $r/R=0.18$ to $r/R=0$ where they report $\chi_e \approx 13\,(\rho_e/L_T)\rho_e v_{te}$.

Following Jenko and Dorland, we seek an operating point for this ETG benchmarking exercise at which the strength of the ETG turbulence is moderate while retaining the full physics of toroidal plasmas (*e.g.*, trapped particles). Jenko and Dorland[13] report that the heat transport due to ETG turbulence drops substantially as the magnetic shear is reduced. This motivated our benchmarking exercise at an operating point defined by $R_0/L_T=6.9$, $R_0/L_n=2.2$, $T_e/T_i=1.0$, $q=1.4$, and $s=0.1$. The simulations are performed with kinetic electrons including only electrostatic fields. Motivated by the large ion gyroradius compared to the expected perpendicular scale of ETG turbulence, we take the ion response to be adiabatic both within and across flux surfaces (that is, $\delta n_i/n_0=-q_i\phi/T$). The simulations are performed in flux-tube geometry with circular plasma cross-section and constant magnetic curvature. As discussed in Sec. III following, the gyrokinetic code results for this operating point are well converged in all numerical parameters except the perpendicular flux-tube cross-section and grid resolution. Hence, efforts to reproduce the ETG benchmark reported here should be performed with flux-tube cross-section $L_x=100\ \rho_e$ and $L_y=64\ \rho_e$, and should employ a radial grid spacing $\Delta x \leq 2\rho_e$, and sufficient resolution in the bi-normal (y) direction to resolve fluctuations out to $k_y\rho_e=0.7$. We find that χ_e increases with both flux-tube cross-section and spatial resolution in the bi-normal (y) direction.

These parameters differ from those employed in the Cyclone ITG benchmarking exercise[8] only in that the magnetic shear, s, has been reduced from 0.79 to 0.1. While this reduction in the magnetic shear produces only a minor change in the linear growth spectrum (the maximum linear growth rate decreases from $\gamma_{max}\approx 0.04\ v_{te}/L_T$ at $s=0.79$ to

$\gamma_{max} \approx 0.037\ v_{te}/L_T$ at $s=0.1$), the heat transport produced by the resulting ETG turbulence drops by about two orders of magnitude. The linear dispersion relation at this operating point is shown in Fig. 1

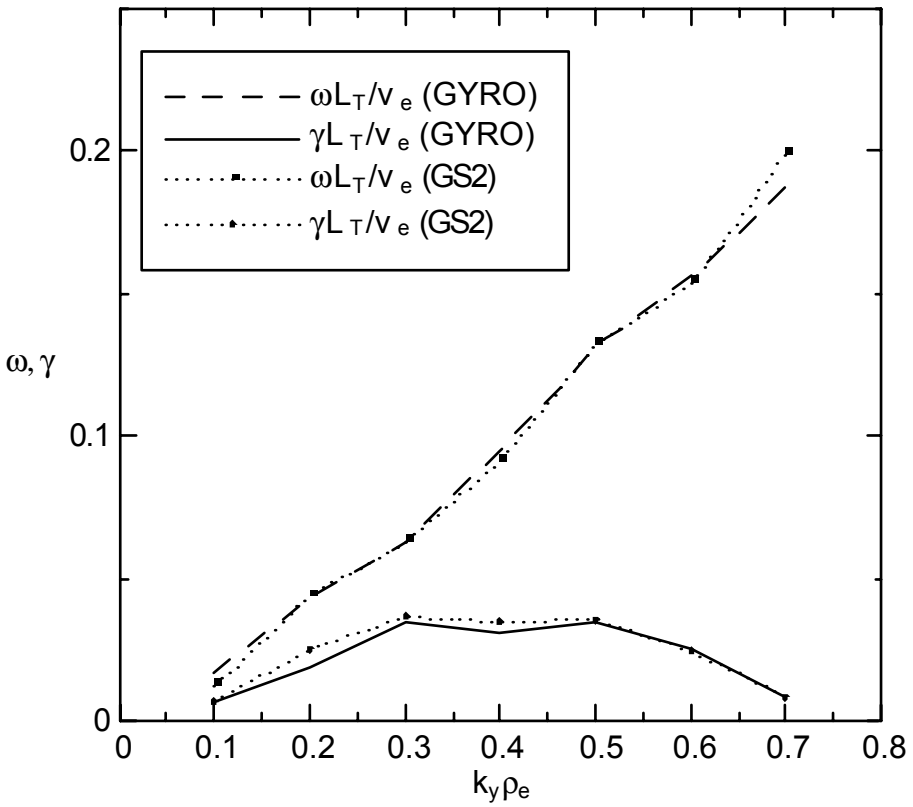

Figure 1 Linear dispersion relation of ETG modes at the benchmark operating point vs. $k_y\rho_e$ as computed by GYRO and GS2 for linear eigenmodes with ballooning mode angle $\theta_0=0$.

The linear growth rate for the ETG modes decreases with increasing ballooning mode angle θ_0, or, equivalently, with increasing midplane radial wavenumber, $k_{r0}\rho_e = sk_y\rho_e\theta_0$. However, this is quite a weak effect, resulting in a decrease in the growth rate of less than 10% over the full range of ballooning mode angle ($-\pi \le \theta_0 \le \pi$) due to the low value of magnetic shear at our benchmark operating point.

The linear eigenmodes for the benchmark operating point are shown in Fig. 2a-b. The structure of these eigenmodes on the interval $-\pi \le \theta \le \pi$ is only weakly dependent on $k_y\rho_e$. In each case the full-width at half-maximum of the eigenfunction in poloidal angle is about π radians. However, the rate at which the eigenfunction falls off at larger values of θ decreases with decreasing $k_y\rho_e$.

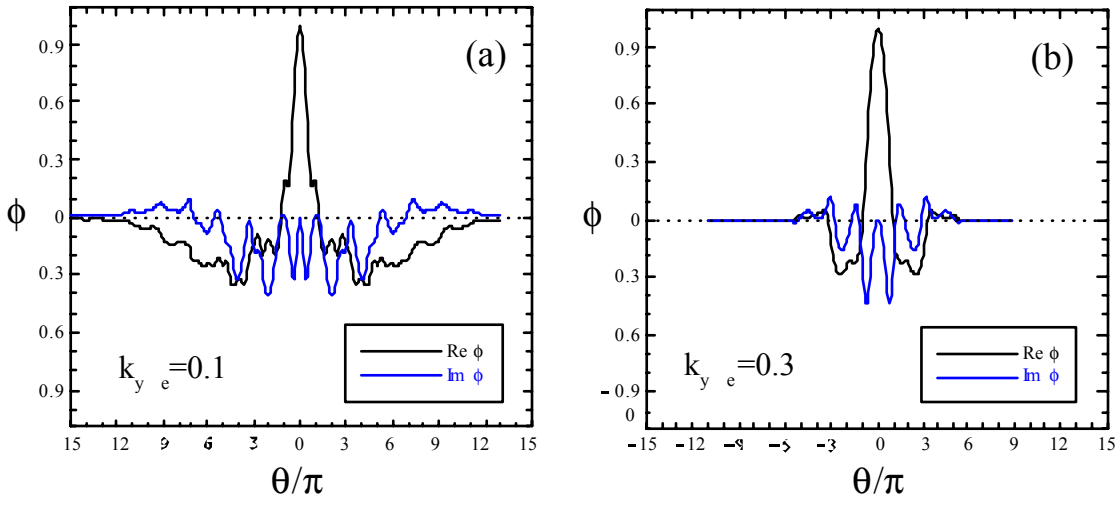

Figure 2 (Color online). The linear eigenfunctions from GYRO are plotted vs. θ for $\theta_0=0$ and (a) $k_y\rho_e=0.1$ (b) $k_y\rho_e=0.3$. In both cases the real part is shown in black and the imaginary part is shown in blue. The eigenfunctions are normalized to equal 1.0 at $\theta=0$.

III. Convergence Studies

Convergence studies reveal any dependency of the simulation results on the numerical parameters determining the resolution in time, configuration space, velocity space, and dimensions of the simulation volume. Convergence tests with the GYRO code were performed by varying specific parameters about a reference simulation at the benchmark

operating point described in Sec. II above. The time-step in the reference GYRO simulation is $dt = 0.025\ a/v_{te} \approx 0.063\ L_T/v_{te}$. The k-space resolution is determined by the flux-tube cross-section $L_x=101.86\ \rho_e$ and $L_y=64\ \rho_e$. There are 50 radial grid points providing a grid resolution of $\Delta r \approx 2\ \rho_e$. GYRO employs a Fourier representation in toroidal angle, retaining 8 Fourier modes in the base-case simulations, which provides resolution out to $k_\perp \rho_e \approx 0.69$ at the outboard midplane. Velocity space is represented using a grid with 8 energies, 8 angles (four trapped and four passing), and two signs of the parallel velocity for a total of 128 velocity classes at each spatial grid point. The reference case for the PG3EQ simulations employs a time step $dt = 0.05\ L_T/v_{te}$ and a flux tube cross-section $L_x=101.86\rho_e$ by $L_y=64\rho_e$. The grid-spacing is $dx=0.795775\rho_e$ by $dy=\rho_e$. Variations along $\boldsymbol{B}$ are represented with 32 grid points. Velocity space is sampled with 16 particles/grid cell.

Figure 3 shows the results of convergence tests about the reference operating point. Demonstrating well-converged results from a single code provides a sufficient basis for this benchmarking exercise. However, given the controversy over ETG simulation results from continuum and PIC codes, we have chosen to present convergence studies from both the continuum code GYRO and the PIC code PG3EQ. These convergence tests examine variations in $\chi_e \equiv -Q_e/n_0 \nabla T_0$ (where Q_e is the volume-averaged electron heat flux while n_0 and ∇T_0 are the equilibrium density and the equilibrium temperature gradient) as numerical parameters of these simulations are varied. We conclude from Fig. 3 that both the GYRO and PG3EQ codes are converged in time-step (this is not an issue for the GENE and GS2 codes as they have automatic time-step control) and

velocity-space resolution. In addition, GYRO is converged in spatial resolution in both the radial and poloidal (along the field-line) directions.

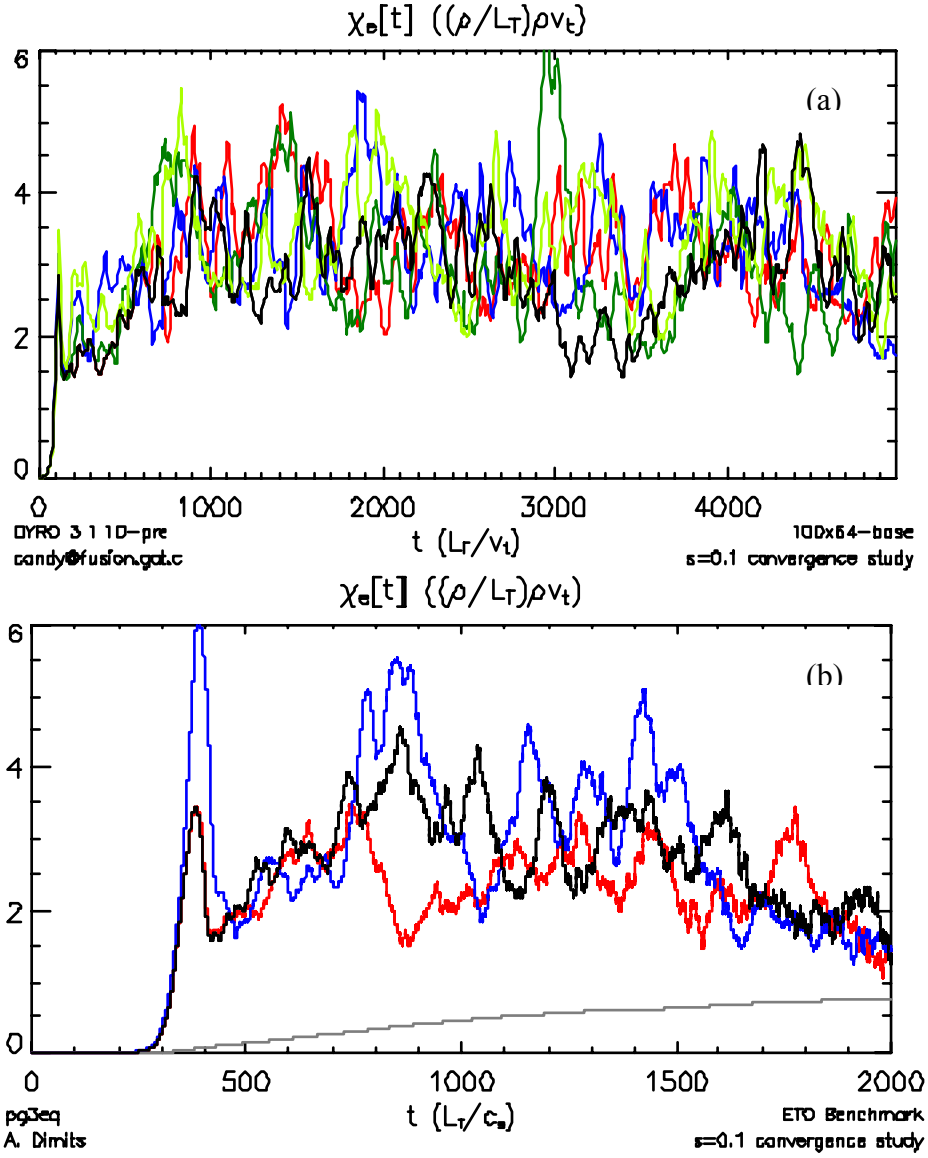

Figure 3 (color online). (a) Convergence study at the benchmark point from the GYRO code and (b) from the PG3EQ code. The black curves are the reference simulation. The timestep is reduced by 1/2 for the red curve. The velocity space resolution is increased in the blue curves (from 128 to 288 velocity classes for GYRO; and from 16 to 32 particles/cell in PG3EQ). The green curve in Fig. 3(a) shows the effect of decreasing the radial grid spacing from $dr \approx 2\rho_e$ to $dr \approx 1.5\rho_e$ in GYRO, while the chartreuse curve shows the effect of increasing the poloidal resolution. The grey curve in Fig. 3(b) shows the contribution of the discrete particle noise to the total heat transport in the PG3EQ simulation.[21]

Convergence with grid spacing in the bi-normal direction (*i.e.*, the direction within the flux surface perpendicular to ***B***) is more problematic. We investigated this issue by comparing GYRO and GENE simulations in which the spatial resolution in the bi-normal is increased by increasing the number of Fourier modes at fixed flux-tube cross-section from 8 Fourier modes for a bi-normal resolution of $k_{y,max}\rho_e=0.7$ (the reference case employed above), to 16 Fourier modes ($k_{y,max}\rho_e=1.5$), and finally 32 Fourier modes ($k_{y,max}\rho_e=3.1$) in the bi-normal (see Fig. 4). The GENE simulations represented variations along ***B*** with 16 grid points, while velocity space is represented with 32 parallel velocities and 8 magnetic moments, for a total of 256 velocity classes at each spatial grid point. The flux-tube cross-section in these GENE simulations was $L_x=100\rho_e$ by $L_y=62.82\rho_e$.

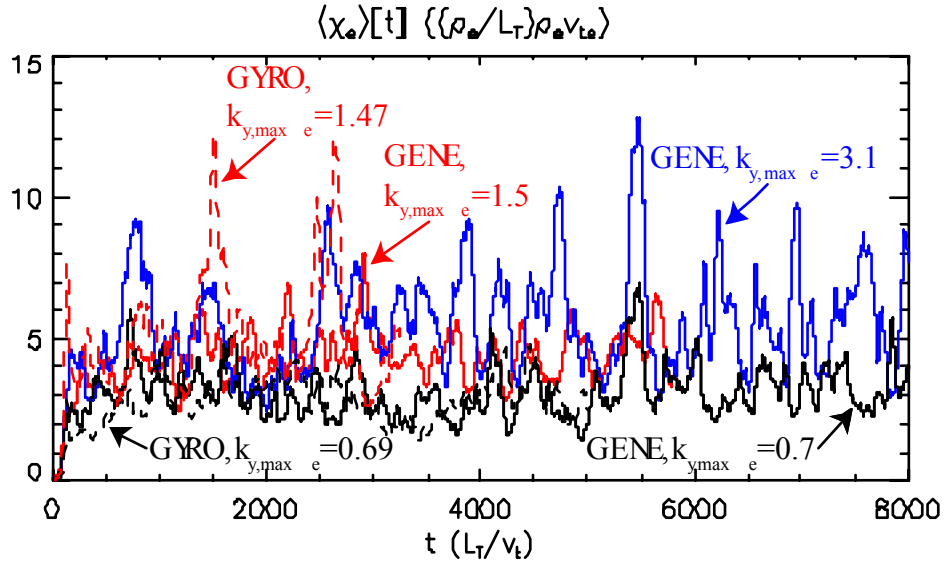

Fig. 4 (Color online). Convergence at the benchmark point in perpendicular grid resolution is investigated by comparing GENE simulations in an $L_x=100\ \rho_e$ by $L_y=62.82\ \rho_e$ flux-tube with 8 bi-normal modes such that $k_{y,max}\rho_e=0.7$ (black curve), 16 k_y-modes such that $k_{y,max}\rho_e=1.5$ (red curve), and 32 k_y-modes such that $k_{y,max}\rho_e=3.1$ (blue curve). Gyro simulations with 8 k_y-modes such that $k_{y,max}\rho_e=0.69$ (dashed black curve) and 16 k_y modes such that $k_{y,max}\rho_e=1.47$ (dashed red curve) are shown for comparison.

We find that our reference case with 8 Fourier modes in the bi-normal is not converged in bi-normal resolution (see Table I). Averaging χ_e over $t > 1000\ L_T/v_{te}$ the 8-mode GENE and GYRO simulations are in agreement with $\langle\chi_e\rangle \approx 2.95(\rho_e/L_T)\rho_e v_{te}$ (GENE, $k_{y,max}\rho_e=0.7$) and $\langle\chi_e\rangle \approx 2.94\ (\rho_e/L_T)\rho_e v_{te}$ (GYRO, $k_{y,max}\rho_e=0.69$). When the resolution in the bi-normal direction is doubled (so that the maximum bi-normal wavenumber resolved increases from $k_{y,max}\rho_e\approx0.7$ to $k_{y,max}\rho_e\approx1.5$) we find that $\langle\chi_e\rangle$ increases by 74%. The GENE and GYRO simulation codes agree on the magnitude of the electron heat transport in this intermediate resolution case, with GENE finding $\langle\chi_e\rangle \approx 5.13\ (\rho_e/L_T)\rho_e v_{te}$ (see line 3 of Table 1) and GYRO finding $\langle\chi_e\rangle \approx 5.41\ (\rho_e/L_T)\rho_e v_{te}$ (see line 4 of Table 1). Comparing this intermediate resolution GENE simulation (which employed 16 Fourier modes in the bi-normal and resolved out to $k_{y,max}\rho_e=1.5$) to the high resolution GENE simulation (which employed 32 Fourier modes and resolved out to $k_{y,max}\rho_e\approx3.10$) we find that $\langle\chi_e\rangle$ increases only another 10% to $\langle\chi_e\rangle \approx 5.66\ (\rho_e/L_T)\rho_e v_t$ — less than the sum of the error bars on our estimates of $\langle\chi_e\rangle$ (compare lines 3 and 6 of Table 1). We conclude that convergence in bi-normal resolution is achieved with 16 or more Fourier modes. That is, bi-normal resolution to $k_{y,max}\rho_e > 1.4$ is required for convergence. Taking the time interval weighted average of $\langle\chi_e\rangle$ from all simulations with $k_{y,max}\rho_e > 1.4$ we estimate the converged value of the electron heat flux in a $100\rho_e \times 64\rho_e$ flux-tube as $\langle\chi_e\rangle = 5.45\pm0.19\ (\rho_e/L_T)\rho_e v_{te}$.

The radial resolution was varied along with the bi-normal resolution in this bi-normal resolution convergence study. Varying the radial grid resolution at the highest bi-normal resolution we find that $\langle\chi_e\rangle$ is insensitive to the radial resolution for $k_{x,max}\rho_e > 1.5$, (see lines 4 thru 6 of Table I).

Table I. Convergence in bi-normal resolution

Code/resolution	$k_{x,max}\rho_e$	$k_{y,max}\rho_e$	$\langle\chi_e\rangle$
1) GENE, reference	2.0	0.70	2.95±0.15 $(\rho_e/L_T)\rho_e v_{te}$
2) GYRO, reference	~0.79	0.69	2.94±0.11 $(\rho_e/L_T)\rho_e v_{te}$
3) GENE, intermediate	4.0	1.50	5.13±0.30 $(\rho_e/L_T)\rho_e v_{te}$
4) GYRO, intermediate	~1.57	1.47	5.41±0.16 $(\rho_e/L_T)\rho_e v_{te}$
5) GENE, high resolution	2.0	3.10	5.48±0.18 $(\rho_e/L_T)\rho_e v_{te}$
6) GENE, high resolution	3.0	3.10	5.66±0.23 $(\rho_e/L_T)\rho_e v_{te}$

Table I. The average of $\chi_e(t)$ over the interval from $t=1000\ L_T/v_{te}$ to the end of the run for GENE and GYRO simulations used in the bi-normal resolution convergence study. The radial resolution for GYRO, which employs finite difference techniques in the radial dimension, is estimated as $k_{x,max}\rho_e \approx \pi/(2\Delta x)$.

We investigate convergence with respect to flux tube cross section at a bi-normal resolution of $k_{y,max}\rho_e=0.69$. Simulations at this reference operating point are reasonably well converged in flux-tube cross-section. Figure 5 shows a sequence of four GYRO simulations in which the flux-tube cross-section is increased from ($L_x=100\rho_e$, $L_y=64\rho_e$) to ($L_x=256\rho_e$, $L_y=256\rho_e$).

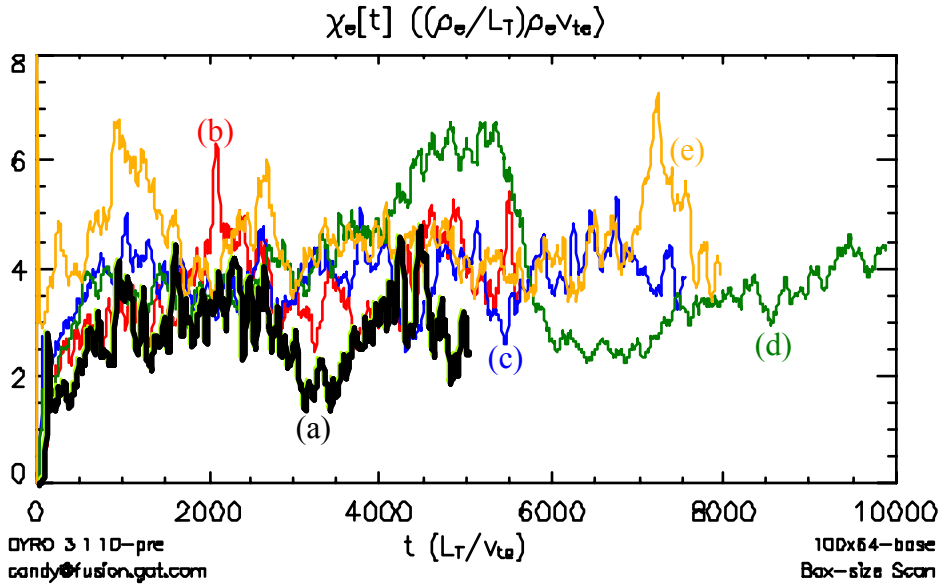

Figure 5 (Color online). The electron thermal conductivity, $\chi_e(t)$, from a sequence of GYRO simulations in which the flux-tube cross section, $L_x \times L_y$, varies from (a) $100\rho_e \times 64\rho_e$ (black curve), thru (b) $128\rho_e \times 128\rho_e$ (red curve) and (c) $256\rho_e \times 128\rho_e$ (blue curve), to (d) $256\rho_e \times 256\rho_e$ (green curve). (e) The simulation at $256\rho_e \times 128\rho_e$ is repeated using kinetic (instead of adiabatic) ions (gold curve).

We see that $\langle\chi_e\rangle$ increases slowly with increasing flux-tube cross-section. The time-averages of $\chi_e(t)$ over the interval $t > 1000\ L_T/v_{te}$ are presented in Table II. The dependence of $\langle\chi_e\rangle$ on the bi-normal dimension of the flux-tube, L_y, is reasonably well fit by $\langle\chi_e\rangle \approx 2.77+0.0074*L_y/\rho_e$, where $\langle\chi_e\rangle$ is in units of $(\rho_e/L_T)\rho_e v_{te}$. A comparison between runs (b) $128\rho_e \times 128\rho_e$ and (c) $256\rho_e \times 128\rho_e$ reveals little dependence of $\langle\chi_e\rangle$ on the radial dimension of the flux-tube, L_x; while a comparison between runs (c) $256\rho_e \times 128\rho_e$ (adiabatic ions) and (e) $256\rho_e \times 128\rho_e$ (kinetic ions) reveals that replacing adiabatic ions with kinetic ions (using a mass ratio of $m_i/m_e=400$) makes very little difference in $\langle\chi_e\rangle$.

Table II $\langle\chi_e\rangle$ vs. Flux-Tube Cross-Section

Flux-tube Cross-section	L_x	L_Y	χ_e
(a) $100\rho_e \times 64\rho_e$, adiabatic ions	$100\rho_e$	$64\rho_e$	2.94±0.11 $(\rho_e/L_T)\rho_e v_{te}$
(b) $128\rho_e \times 128\rho_e$, adiabatic ions	$128\rho_e$	$128\rho_e$	3.76±0.08 $(\rho_e/L_T)\rho_e v_{te}$
(c) $256\rho_e \times 128\rho_e$, adiabatic ions	$256\rho_e$	$128\rho_e$	3.86±0.07 $(\rho_e/L_T)\rho_e v_{te}$
(d) $256\rho_e \times 256\rho_e$, adiabatic ions	$256\rho_e$	$256\rho_e$	4.51±0.11 $(\rho_e/L_T)\rho_e v_{te}$
(e) $256\rho_e \times 128\rho_e$, kinetic ions	$256\rho_e$	$128\rho_e$	3.96±0.24 $(\rho_e/L_T)\rho_e v_{te}$

Table II. The average of $\chi_e(t)$ over the interval from $t=1000 v_{te}/L_T$ to the end of the simulation for the flux-tube cross-section scan shown in Fig. 5.

The tendency for χ_e to increase with bi-normal extent of the simulation, L_y, leads us to examine the fluctuation spectrum in an effort to understand why box-size convergence is proving elusive. Figure 6 shows that the fluctuation spectrum converges with increasing L_y at large $|k|$ ($|k\rho_e| > 0.2$), where it falls off as $|\phi(k)|^2 \sim 1/k^2$. Figure 6a shows that below $k_y\rho_e \approx 0.2$ the k_y-spectrum fails to converge with the box-size because the intensity increases at low k_y as the box-size is increased. In contrast, Fig. 6b shows that the k_r-spectrum is well-behaved at small $k_r\rho_e$. The divergence of the k_y-spectrum as $k_y\rho_e \to 0$ explains the lack of convergence with increasing L_y, while the absence of this divergence in the k_r-spectrum allows convergence as L_x is increased.

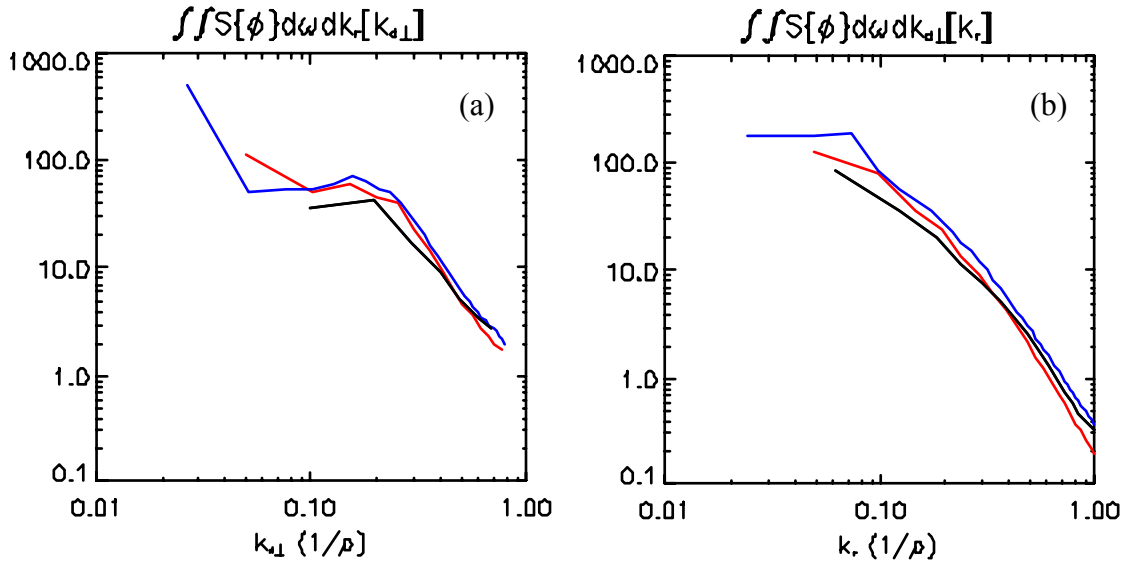

Fig. 6 (Color online). Fluctuation spectrum of the electrostatic potential at the outboard mid-plane is plotted (a) vs. the wavenumber in the bi-normal direction and (b) vs. wavenumber in the radial direction for GYRO runs with flux-tube cross section $L_x=100\rho_e$ by $L_y=64\rho_e$ (black curve); $L_x=128\rho_e$ by $L_y=128\rho_e$ (red curve) and $L_x=256\rho_e$ by $L_y=256\rho_e$ (blue curve).

This same information can be cast in terms of the correlation function. Figure 7a shows the correlation function vs. the bi-normal separation, while Fig. 7b shows the correlation function vs. the radial separation. The correlation function is well-converged for $L_x \geq 125\rho_e$ at separations less than about $10\ \rho_e$ (corresponding to large $k_\perp$) in both bi-normal and radial directions. However, the fall off at large separation decreases as the flux-tube cross section is increased, reflecting the presence of significant fluctuation intensity in long wavelength modes.

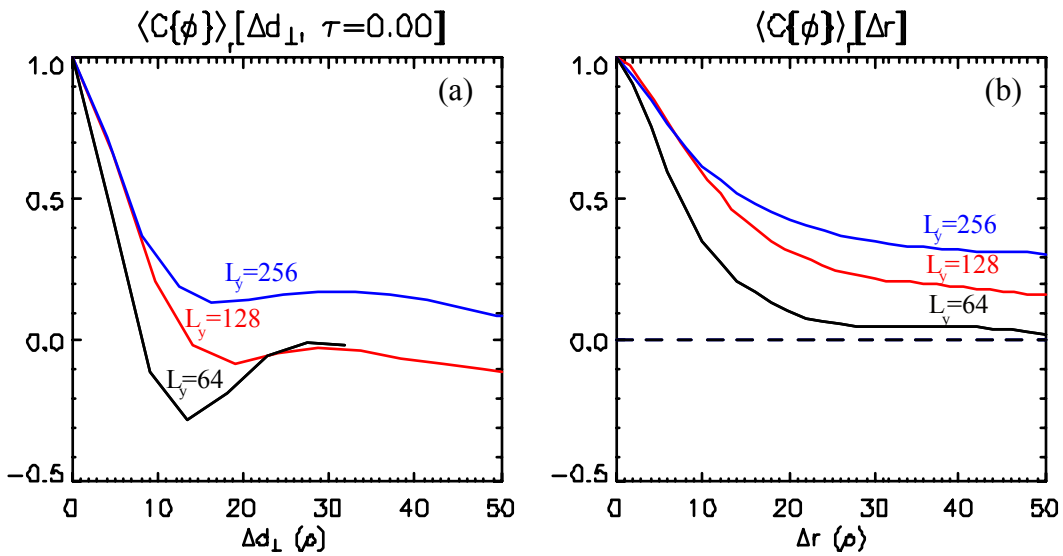

Figure 7 (Color online). The correlation function of the midplane potential is plotted (a) vs. separation in the binormal direction and (b) vs. separation in the radial direction for GYRO simulations with flux-tube cross sections of $L_x=100\rho_e$ by $L_y=64\rho_e$ (black curve), $L_x=128\rho_e$ by $L_y=128\rho_e$ (red curve) and $L_x=256\rho_e$ by $L_y=256\rho_e$ (blue curve).

The convergence in flux-tube cross section would be improved if the benchmark operating point were modified such that there was a long wavelength cut-off in the fluctuation spectrum. This might be accomplished within the adiabatic ion/kinetic electron model employed here by choosing a more realistic magnetic geometry with good average curvature (the flux-surface average curvature for the magnetic geometry considered here is exactly zero), or by including electromagnetic fields in the expectation that they may provide a long wavelength cut-off at $k_y c/\omega_{pe}\approx 1$. More generally, it has already been demonstrated that replacing the adiabatic ion model with kinetic ions provides the long wavelength dynamics required to achieve proper box-size convergence.[13,30]

IV. Cross-code Comparisons

Having demonstrated that our gyrokinetic simulation codes are well-behaved at the chosen operating point, we now turn to cross-code comparisons. Gyrokinetic simulations of ETG turbulence have been performed at the benchmark point described in Sec. II with the continuum gyrokinetic codes GYRO,[23] GS2,[14] and GENE;[13] and the particle-in-cell code PG3EQ.[7] The electron thermal conductivity results, $\chi_e \equiv -Q_e/n_0 \nabla T_0$, from GYRO, GS2, GENE, and PG3EQ are plotted versus time in Fig 8.

The numerical resolution in GYRO, PG3EQ and GENE is as described for the reference case in Sec. III above. The GS2 code adjusts its time step to insure accuracy of the time integration. It was run with a flux-tube cross-section of $L_x=101.8\rho_e$ and $L_y=64\rho_e$. GS2 employs a Fourier representation in the plane perpendicular to $\boldsymbol{B}$ with 21 radial modes, 11 modes in the bi-normal, and 30 grid-points along $\boldsymbol{B}$. Velocity space was represented with 8 energies by 36 angles and two signs of the parallel velocity for a total of 576 velocity classes at each spatial grid point.

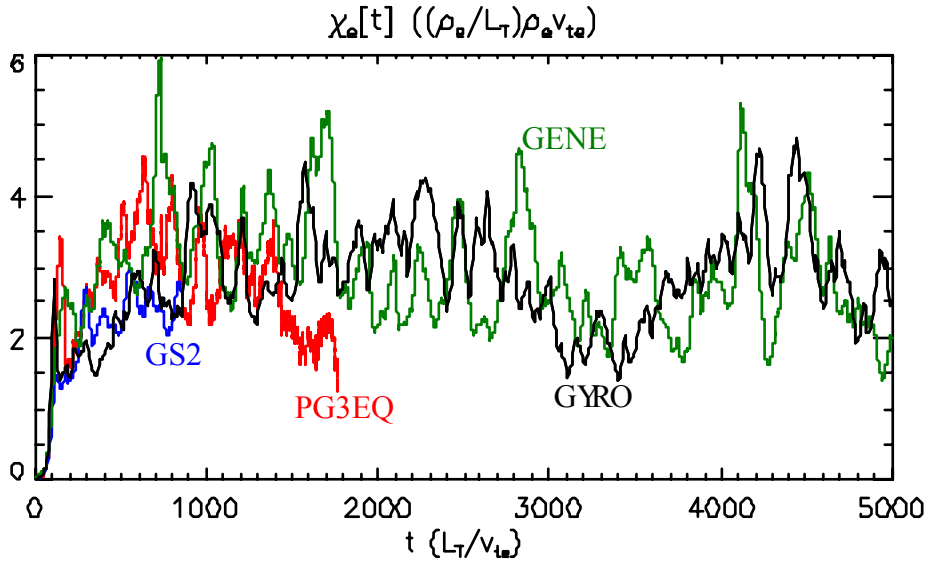

Figure 8 (color online). $\chi_e \equiv -Q_e/n_0 \nabla T_0$, from GYRO (black curve), GS2 (blue curve), GENE (green curve), and PG3EQ (red curve) are plotted versus time.

Averaging $\chi_e(t)$ over the maximum interval of steady-state turbulence in each code ($500 < t < 5000$ for GYRO; $300 < t < 873$ for GS2; $500 < t < 10000$ for GENE; and $500 < t < 2000$ for PG3EQ) we find $\langle\chi_e\rangle_{GYRO}=2.93\ (\rho_e/L_T)\rho_e v_{te}$, $\langle\chi_e\rangle_{GS2}=2.38\ (\rho_e/L_T)\rho_e v_{te}$, $\langle\chi_e\rangle_{GENE}=2.98\ (\rho_e/L_T)\rho_e v_{te}$, and $\langle\chi_e\rangle_{PG3EQ}=2.85\ (\rho_e/L_T)\rho_e v_{te}$, for a (time-interval) weighted average and standard deviation of $\langle\chi_e\rangle = 2.93\pm0.11\ (\rho_e/L_T)\rho_e v_{te}$. The time-interval weighted standard deviation in $\langle\chi_e\rangle$ between codes yields an error in our estimate of the mean of less than 10%. This agreement between codes is better than that achieved in the Cyclone ITG benchmarking exercise.[8]

The electron thermal transport is the quantity of greatest macroscopic interest. However, a detailed code benchmarking also requires a comparison of the microscopic fluctuations. These fluctuations can be characterized by the fluctuation intensity averaged over the outboard midplane, $\langle\delta\phi^2\rangle$, the 2-point correlation function of $\delta\phi$,

$$C\{\delta\phi\} \equiv \frac{\left\langle \delta\phi(\vec{x}+\Delta, t-\tau)\delta\phi(\vec{x},t)\right\rangle}{\left\langle \delta\phi(\vec{x},t)^2\right\rangle}\ , \tag{1}$$

and the spectral density,

$$S\{\delta\phi\} \equiv \left\langle \left|\delta\phi(k,\omega)\right|^2 \right\rangle. \tag{2}$$

The ETG fluctuations are isolated from the *n=0* modes (zonal flows and geodesic-acoustic modes which do not produce any radial transport) by defining $\delta\phi$ to be the deviation of the mid-plane potential from its toroidal average.

Figure 9 displays the ETG fluctuation intensities from GYRO, GS2, and PG3EQ. The late-time ($t > 900\ L_T/v_{te}$) drop in the ETG fluctuation intensity from PG3EQ is probably due to the accumulation of discrete particle noise.[21] We see that the intensity of the ETG turbulent fluctuations from each of these codes is substantially the same.

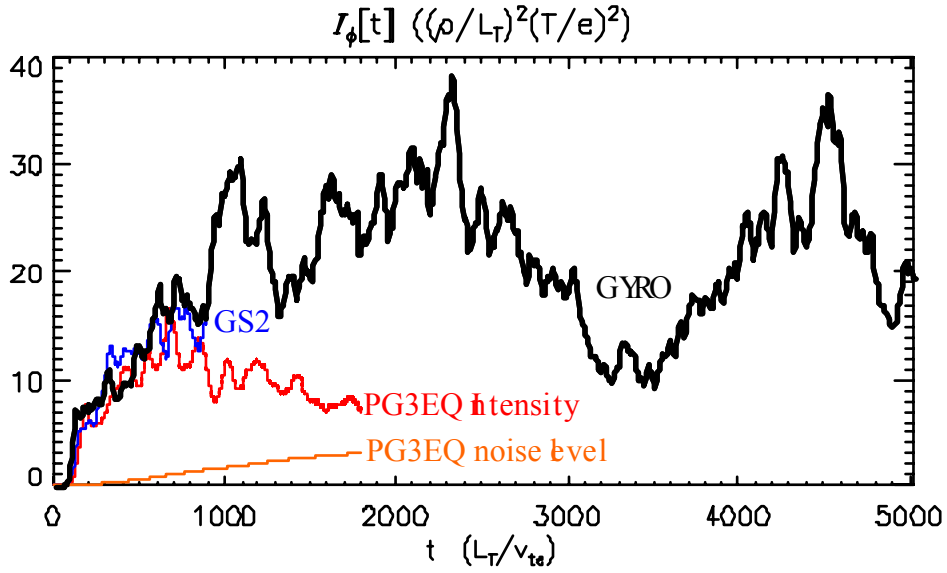

Figure 9 (Color online). The fluctuation intensity, $\langle \delta\phi^2 \rangle$, averaged over the outboard midplane from GYRO (black curve), GS2 (blue curve) and PG3EQ (red curve). The contribution of discrete particle noise to the PG3EQ fluctuation intensity is shown by the orange curve.

Figures 10 (a) and (b) display estimates of $C\{\delta\phi\}$ from the GYRO, PG3EQ, and GS2 benchmark runs as a function of both the spatial separation, Δ, and the time-lag, τ. These estimates of the correlation function are seen to be in substantial agreement. Defining the radial correlation length, ℓ_r, as the full-width at half-maximum of the correlation function vs. the radial separation, we find $\ell_r \approx 17.5 \pm 1.0\ \rho_e$. Similarly, the transverse eddy width, $\ell_\perp$, is defined as the full-width at half-maximum of the correlation function vs. the bi-normal separation. We find $\ell_\perp \approx 9.1 \pm 1.01\ \rho_e$. That is, a typical turbulent eddy has a mild radial elongation with an aspect ratio of about 2, similar to previous simulations of ETG turbulence.[32] The eddy lifetime, τ_{Eddy}, is defined as the full-width at half-maximum of the correlation function vs. time lag, where the spatial separation is chosen at each value of τ so as to maximize $C\{\delta\phi\}$. This somewhat more complex procedure is chosen

because the turbulent eddies propagate (mainly in the bi-normal direction) and it is our goal to characterize the lifetime of a typical turbulent eddy rather than the time required for a typical turbulent eddy to move past a stationary observer (which would be given by the full-width at half maximum of $C\{\delta\phi\}$ vs. τ evaluated at $\Delta=0$). We find $\tau_{Eddy}\approx 100\pm 10\ L_T/v_{te}$.

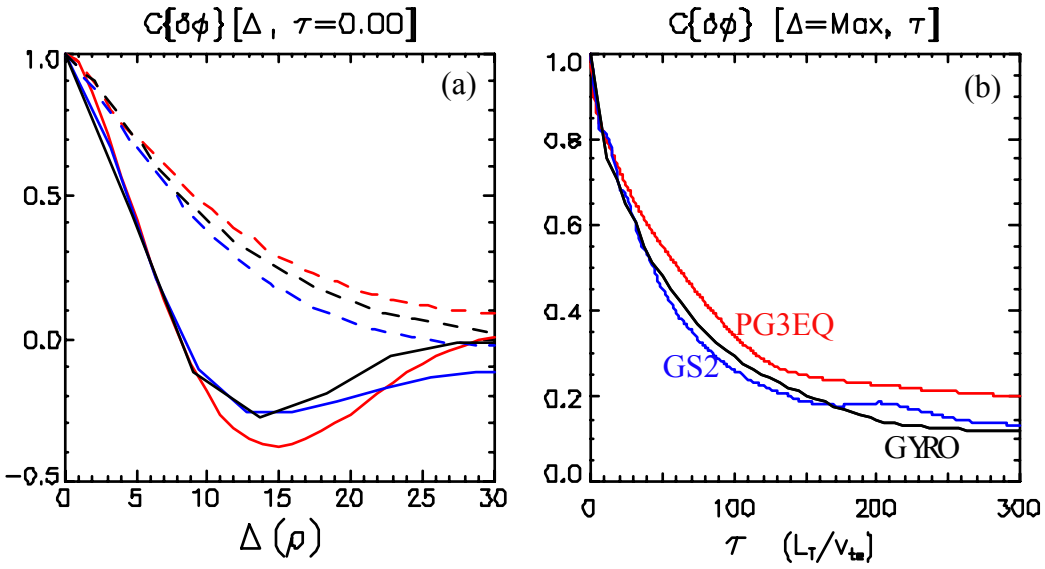

Figure 10 (Color online). (a) The 2-point correlation function from GYRO (black curves), GS2 (blue curves), and PG3EQ (red curves) is displayed as a function of the bi-normal separation (solid curves) and the radial separation (dashed curves) at $\tau=0$. (b) The 2-point correlation function is displayed as a function of the time-lag. The spatial separation, Δ, is chosen at each value of τ so as to maximize $C\{\delta\phi\}$.

The fluctuation spectrum in the $(k_r,\ k_\perp)$-plane is markedly anisotropic at low wave-number ($|k\rho_e| < 0.2$), with $k_\perp$ generally larger than k_r. At larger wave-number ($|k\rho_e| > 0.2$) the spectrum becomes isotropic in the plane perpendicular to $\boldsymbol{B}$ [see Fig. 11(a)]. Considered as a function of frequency and bi-normal wave number, $k_\perp$, we see that the turbulent fluctuations are generally well-organized at lower $k_\perp$ ($k_\perp\rho_e < 0.2$) in the sense that they have a well-defined frequency as a function of $k_\perp$, such that

$\omega \approx 0.2(\rho_e/L_T)k_\perp v_{te}$. At larger wave-numbers ($k_\perp\rho_e > 0.2$) the turbulent fluctuations are disorganized, such that the frequency is no longer well-defined as a function of the wavenumber [see Fig. 11(b).

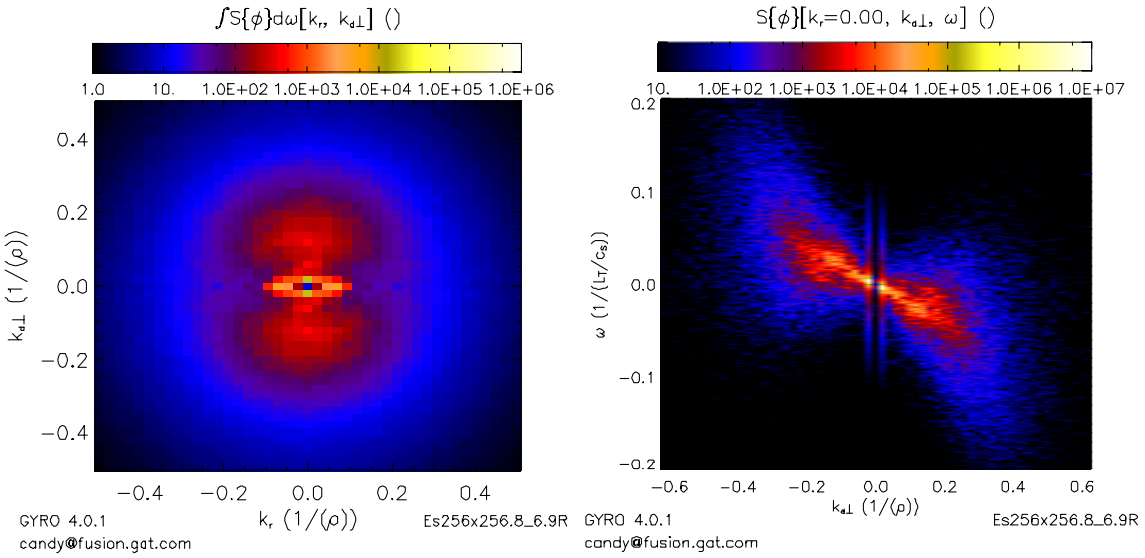

Fig. 11 (color online). Spectral density of electrostatic potential fluctuations at the *s=0.1* benchmark point (a) vs. $(k_r,k_\perp)$ and (b) vs. $(k_\perp, \omega)$.

Having demonstrated that ETG turbulence as characterized by the intensity and correlation function of $\delta\phi$ is substantially the same in the benchmark simulations from GYRO, PG3EQ and GS2, we turn our attention to the *n=0* component of the potential, $\langle\phi\rangle(r,t)$. Considerations of gauge and Galilean invariance imply that the *n=0* component of the potential mainly affects the ETG turbulence and the resulting anomalous transport through the shear in the *n=0* component of the *E×B* flow. Shear in the *E×B* flow leads to decorrelation of the turbulent eddys at a rate proportional to the *E×B* flow shear.[33-35] For the ETG simulations in question there is no externally imposed *E×B* flow shear. We can

characterize the decorrelation due to the time and space-dependent flow shear generated by $\langle\phi\rangle(r,t)$ through the shear decorrelation rate,

$$\Gamma_{E\times B} = \left(\frac{\ell_r}{\ell_\perp}\right)\left\langle\left|\frac{\partial}{\partial r}V_{E\times B}\right|^2\right\rangle^{1/2}, \qquad (3)$$

where ℓ_r and $\ell_\perp$ are the radial and bi-normal correlation lengths of the ETG turbulence defined above, while $\partial V_{ExB}/\partial r$ is the shear in the $E\times B$ flow at spatial scales large compared to the radial eddy width, ℓ_r, and at time scales such that the flow pattern persists for times long compared to the eddy lifetime, τ_{Eddy}. The *rms* flow shear, $\langle|\partial V_{ExB}/\partial r\ |^2\rangle^{1/2}$, is computed using digital filters to remove spatial scales shorter than ℓ_r and time scales shorter than τ_{Eddy} and displayed in Fig. 12. We find that there is substantial agreement between GYRO, PG3EQ and GS2 in the *rms* flow shear, $\langle|\partial V_{ExB}/\partial r\ |^2\rangle^{1/2} \approx 0.027 \pm 0.004\ v_{te}/L_T$.

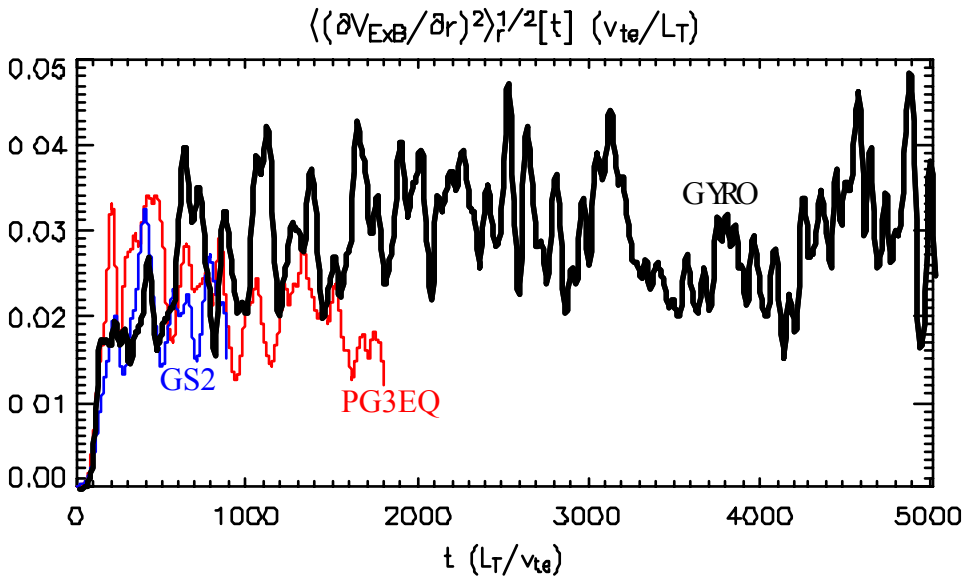

Figure 12 (Color online). The *rms* flow shear is displayed vs. time from GYRO (black curve), PG3EQ (red curve) and GS2 (blue curve).

It follows that the shear decorrelation rate, $\Gamma_{E\times B} \approx 0.054\pm0.01\ v_{te}/L_T$, is comparable to the linear growth rate of the fastest growing mode, $\gamma_{max} = 0.037\ v_{te}/L_T$. This result is similar to that found in gyrokinetic simulations of ETG turbulence in stellerators.[32] Values of the background shear decorrelation rate in excess of the maximum linear growth rate can suppress ITG Turbulence.[5,33] Turbulence-driven zonal flows are known to play a key role in ITG turbulence saturation, where the shearing rate of the zonal flows is comparable to the fastest growing linear ITG mode (see, for example, the gyrofluid simulations in Ref. 35). It is interesting to note that both ETG and ITG turbulence appear to exhibit self-regulation such that $\Gamma_{E\times B} \sim \gamma_{max}$. The ETG simulations reach much larger values of $\chi/\chi_{gyroBohm}$ before achieving this balance because the coupling of ETG modes to zonal flows is weaker than that of ITG modes. At these parameters ITG turbulence

produces transport levels (as measured in ion gyro-Bohms) of $\chi_i \approx 0.6\ (\rho_i/L_T)\ \rho_i v_{ti}$, which are substantially lower than those obtained here for ETG turbulence [$\chi_e \approx 3\ (\rho_e/L_T)\ \rho_e v_{te}$].

V. Magnetic Shear Scan

A key issue for ETG turbulence is whether it is capable of producing a large electron heat flux. The electron thermal conductivity must be larger than about $5\ (\rho_e/L_T)\rho_e v_{te}$ to be consistent with transport analysis from tokamak experiments (see Sec. VI following). Jenko and Dorland's work[13] leads us to expect that there will be a substantial increase in the electron thermal transport as the magnetic shear is increased past $s=0.4$. Figure 13 shows the electron thermal conductivity from a sequence of GYRO and GENE simulations in which the magnetic shear is varied at a bi-normal resolution $k_{y,max}\rho_e=0.69$ (these simulations were performed before we discovered that convergence in bi-normal resolution requires $k_{y,max}\rho_e>1.4$). As the magnetic shear is varied over the range $0.1 \le s \le 0.35$ the initial transient in the heat flux becomes more dramatic while the late-time ($t > 1500\ L_T/v_{te}$ for GYRO simulations and $t > 2500\ L_T/v_{te}$ for GENE simulations) average of χ_e remains substantially unchanged, varying between 2.7 and $3.8\ (\rho_e/L_T)\rho_e v_{te}$. When the magnetic shear is increased further to $s=0.4$ the electron thermal conductivity takes a dramatic jump to $\langle\chi_e\rangle \approx 200\ (\rho_e/L_T)\rho_e v_{te}$ (GYRO) or $73\ (\rho_e/L_T)\rho_e v_{te}$ (GENE).

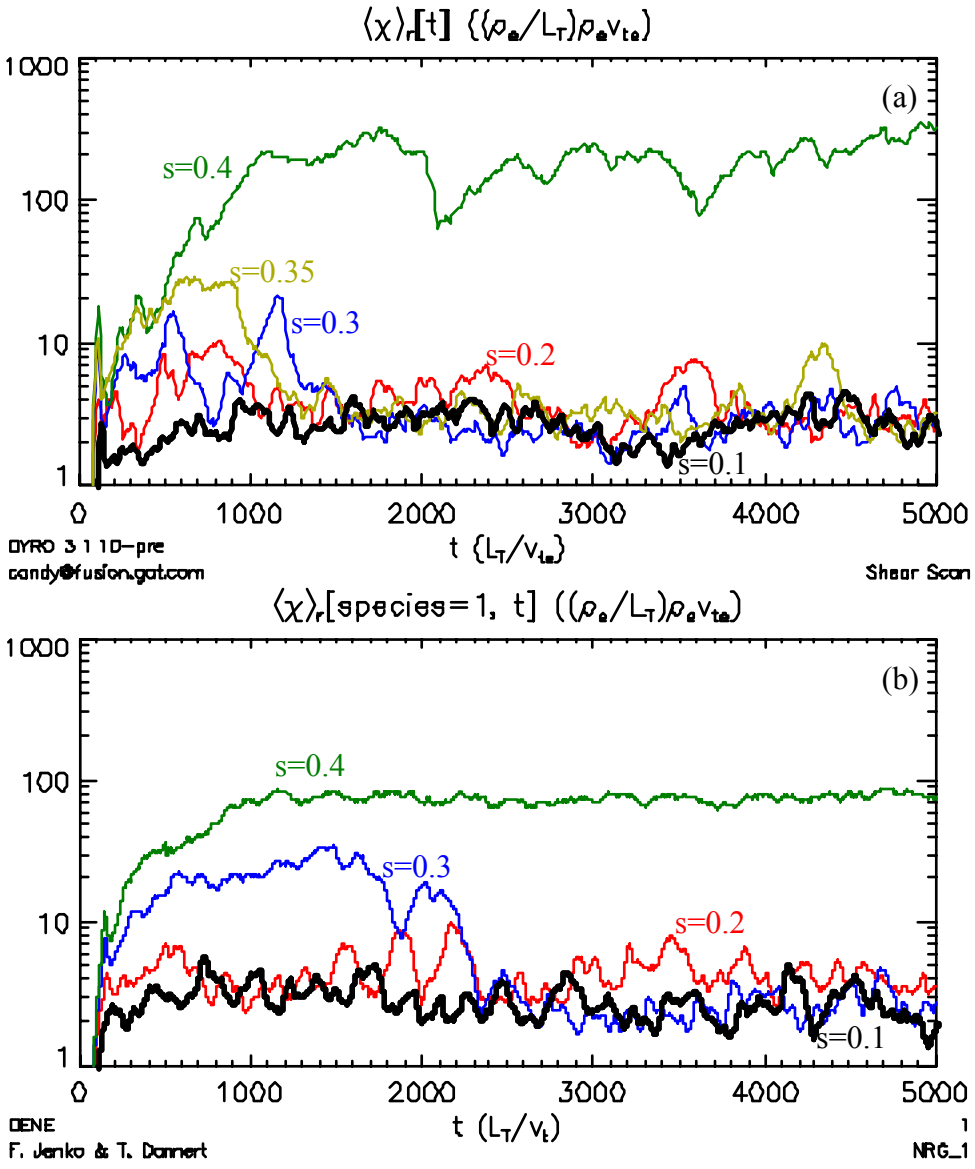

Figure 13 (color online). $\chi_e \equiv -Q_e/n_0 \nabla T_0$, from a sequence of simulations with flux-tube cross-section of $L_x=100\rho_e$ by $L_y=64\rho_e$ using (a) GYRO in which the magnetic shear is varied through $s=0.1$ (black curve), $s=0.2$ (red curve), $s=0.3$ (blue curve), $s=0.35$ (olive curve) and $s=0.4$ (green curve); and (b) GENE in which the magnetic shear is varied through $s=0.1$ (black curve), $s=0.2$ (red curve), $s=0.3$ (blue curve), and $s=0.4$ (green curve).

Substantially similar results are obtained from both GS2 and PG3EQ. In particular, we confirm this dramatic increase in the electron thermal transport at $s=0.4$ by reproducing this simulation with GS2 and PG3EQ as illustrated in Fig. 14 below. These values of χ_e

are much larger than those obtained by Jenko and Dorland[13-15] who performed simulations without trapped particles obtaining $\chi_e \approx 13 \chi_{e,GB}$.

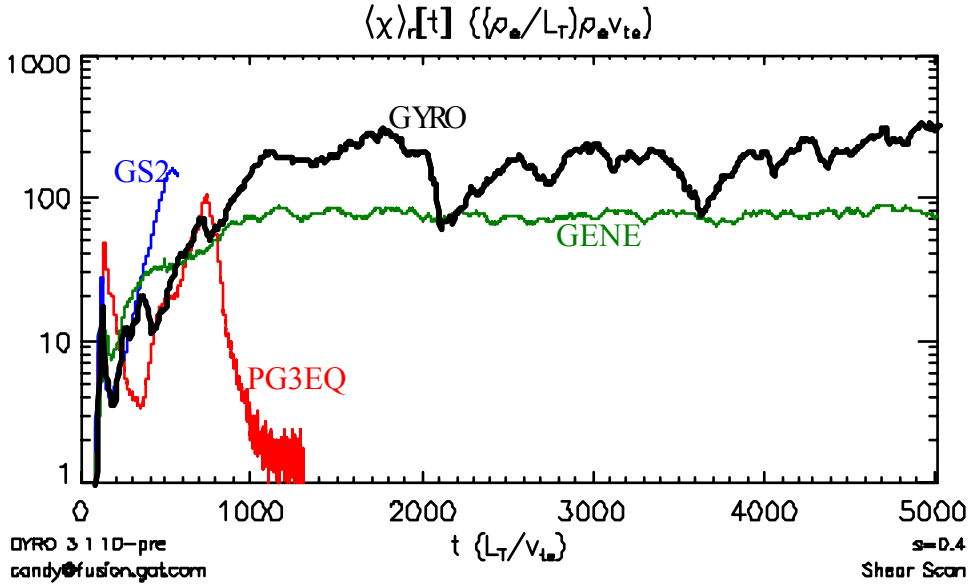

Figure 14 (color online). $\chi_e \equiv -Q_e/n_0 \nabla T_0$ at $s=0.4$ from GYRO (black curve), GS2 (blue curve), GENE (green curve) and PG3EQ (red curve). The late-time ($t > 750\ L_T/v_{te}$) drop in χ_e from PG3EQ is due to the accumulation of discrete particle noise.[21]

When the magnetic shear is increased to $s=0.4$, the spectral density in the $(k_r,k_\perp)$-plane becomes nearly mono-chromatic, with almost all of the intensity concentrated in a single mode at $k_r\rho_e=0$, and $k_\perp\rho_e \approx 0.1$ (this is the longest wavelength in the bi-normal direction allowed by the boundary conditions). Considered as a function of frequency and bi-normal wave number, $k_\perp$, the fluctuations are again well-organized at lower $k_\perp$ ($k_\perp\rho_e < 0.2$) and disorganized at larger wave-numbers ($k_\perp\rho_e > 0.2$).

The transition to a nearly mono-chromatic spectrum occurs abruptly as the magnetic shear is increased and is closely associated with the sharp increase in the electron heat transport as the magnetic shear is increased from $s=0.3$ to $s=0.4$. Very high electron heat

transport [$\chi_e >> 10\ (\rho_e/L_T)\rho_e v_{te}$] is, in our experience, always accompanied by a nearly mono-chromatic fluctuation spectrum with $k_r \approx 0$. This spectrum corresponds to coherent "streamers" with a macroscopic radial scale in the perpendicular plane within configuration space.

This rapid increase in the electron heat transport with increasing shear would appear to be the most dramatic result of our study of ETG turbulence. As such, we employed the GYRO code to repeat the magnetic shear scan with the adiabatic ions replaced by full gyro-kinetic ions at a mass ratio of $m_i/m_e=400$. Figure 15 shows $\chi_e(t)$ from these simulations which employed a somewhat larger flux-tube cross-section, $256\rho_e \times 128\rho_e$, and bi-normal resolution $k_{y,max}\rho_e=0.69$.

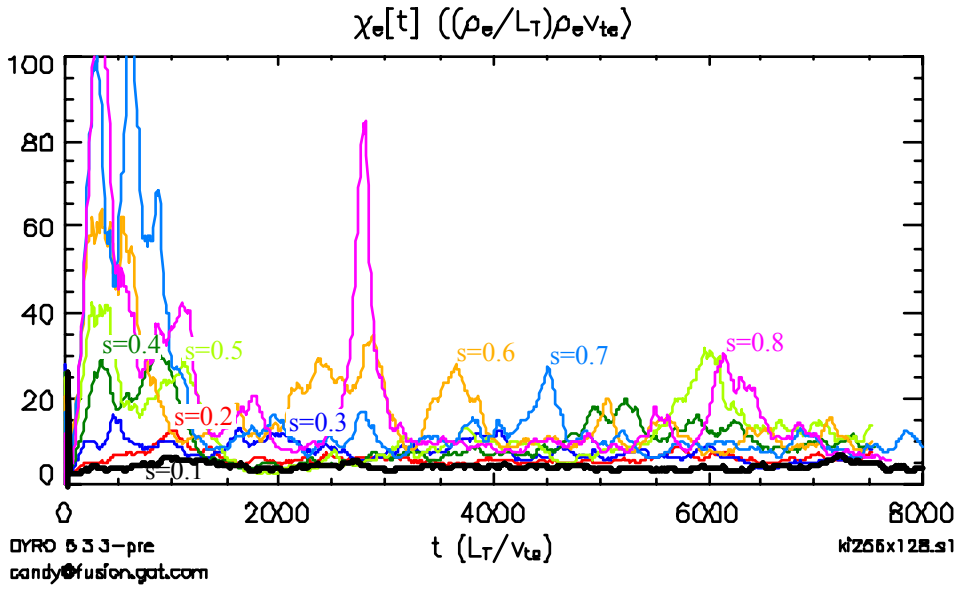

Figure 15 (Color online). The electron thermal transport from a GYRO magnetic shear scan with kinetic ions, including s=0.1 (black curve), s=0..2 (red curve), s=0.3 (blue curve), s=0.4 (green curve), s=0.5 (chartreuse curve), s=0.6 (gold curve), s=0.7 (turquoise curve), and s=0.8 (purple curve).

With kinetic ions the intensity of the initial burst of turbulence increases with increasing magnetic shear (as was the case for adiabatic ions, see Fig. 13 above). However the electron heat flux drops back down so that the late-time average remains modest (see Table III).

Table III. $\langle\chi_e\rangle$ vs. magnetic shear

	s=0.1	s=0.2	s=0.3	s=0.4	s=0.5	s=0.6	s=0.7	s=0.8
Adiabatic ions	3.9±0.1	5.3±0.6	6.8±1.0	10.2±1.3	128±35	> 800	> 800	> 600
Kinetic ions	4.4±0.2	5.5±0.2	7.0±0.6	9.2±1.2	10.7±2.0	14.3±2.2	10.5±0.9	13.6±2.2

Table III. $\langle\chi_e\rangle$ as a function of the magnetic shear from a sequence of GYRO simulations with a flux-tube cross-section of $256\rho_e \times 128\rho_e$ and a bi-normal resolution $k_{y,max}\rho_e=0.69$ using both adiabatic and kinetic ions. The mass ratio was taken to be $m_i/m_e=400$ in the simulations with kinetic ions. The time-average is taken over the interval $2000\ L_T/v_{te} < t < 8000\ L_T/v_{te}$ in all cases except the adiabatic ion run at $s=0.5$, where the average is taken over $2000\ L_T/v_{te} < t < 6200\ L_T/v_{te}$ (where this run terminated). The adiabatic ion simulations with $s > 0.5$ all terminated before $t=1000\ L_T/v_{te}$. At termination in these simulations χ_e took on the value indicated in the table.

Comparing this magnetic shear scan with kinetic ions to a similar scan with adiabatic ions and the same flux-tube dimensions and grid resolution, we find that the adiabatic ion model breaks down when the magnetic shear exceeds s=0.4. Instead of the dramatic increase of $\langle\chi_e\rangle$ with increasing magnetic shear found with the adiabatic ion model, simulations with gyro-kinetic ions show a modest, but steady increase in $\langle\chi_e\rangle$ with increasing magnetic shear over the interval $0.1 \le s \le 0.6$.

These simulations were not converged in bi-normal resolution (they were performed before we uncovered this problem). We anticipate that a magnetic shear scan at higher bi-normal resolution would show a similar trend with $\langle\chi_e\rangle$ increasing with increasing magnetic shear, while the overall magnitude of $\langle\chi_e\rangle$ may be as much as a factor of 2 higher consistent with the 90% increase in $\langle\chi_e\rangle$ observed in our bi-normal convergence study at $s=0.1$. On the other hand, ETG transport may be reduced in the presence of long wavelength ITG/TEM (trapped electron mode) turbulence. The interaction of ETG and ITG/TEM is currently under study and is being reported on elsewhere[31].

VI. Electron transport rates in experiment

Transport analyses of DIII-D,[36] JET,[37] and JT-60U[38] discharges suggest that ETG turbulence may be responsible for the electron heat transport across thermal barriers, in the L-mode edge of discharges with internal transport barriers, and in the outer half of H-mode discharges.[39] For example, scaling experiments on the DIII-D tokamak[39] show that electron and ion heat transport in the outer half of H-mode discharges have different scaling with $\rho^*=\rho/a$, indicating that there is a fundamental difference in the mechanisms responsible for the electron and ion heat transport in these discharges. In this region the electron heat transport is unaffected by changes in the $E\times B$ shearing rate and exhibits nearly gyro-Bohm scaling with ρ^* as one would expect if the electron heat transport

resulted from ETG turbulence. However, the near isomorphism between ITG and ETG turbulence involves exchanging ion scales (the ion gyroradius, ρ_i, and the ion thermal velocity, v_{ti}) for the corresponding electron scales (the electron gyroradius, ρ_e, and the electron thermal velocity, v_{te}). As a result the transport associated with ETG turbulence is measured in electron gyro-Bohms. In deuterium plasmas electron gyro-Bohms are 60 times smaller than the ion gyro-Bohms used to calibrate the ITG turbulence thought to be responsible for much of the energy transport observed in tokamak experiments. This factor of 60 has led to great skepticism regarding the practical significance of ETG turbulence to electron transport in tokamak experiments. These conflicting views can be resolved by calibrating the observed electron heat transport in electron gyro-Bohms and comparing the results to the transport levels observed in the microturbulence simulations of ETG transport reported above. In *mks* units an electron gyro-Bohm is given by

$$\chi_{e,GB} \equiv \left(\frac{\rho_e}{L_T}\right)\rho_e v_{te} \approx 0.075\left[T_e\ (keV)\right]^{3/2}\left[B\ (T)\right]^{-2}\left[L_T\ (m)\right]^{-1}\ \ m^2/s\ . \qquad (4)$$

where T_e is the electron temperature in keV, B is the magnetic field in Tesla, and L_T is the electron temperature scale-length in meters.

The magnitude of the experimentally observed electron thermal conductivity varies with plasma conditions. Of particular interest are discharges with internal transport barriers because the ion-scale turbulence is suppressed by $E\times B$-shear within the barrier while the electron-scale ETG turbulence is largely unaffected by the $E\times B$-shear. Stallard et al[36]

have analyzed several DIII-D discharges with internal transport barriers. They find the measured electron temperature gradient tracks the (linear) marginally stable gradient for ETG modes within the thermal barrier, suggesting that ETG turbulence controls the electron temperature gradient within these thermal barriers. The electron temperature gradient is substantially larger than the marginally stable gradient in the L-mode edge plasma outside of the thermal barrier, so that ETG modes are strongly unstable in this region and may be responsible for the observed electron heat transport. Table V presents values of T_e and L_T from Figs. 1 thru 6 of Ref. 36, together with the experimental electron heat transport calibrated in electron gyro-Bohms both within the thermal barrier and in the L-mode edge.

Table V. DIII-D Electron transport analysis

	$\chi_e/\chi_{e,GB}$	T (keV)	L_T (m)
Fig. 1 & 2, t=1.82s, *r/a=0.35*	0.84	3.5	0.17
Figs. 4, 5 & 6, *r/a=0.35*	0.16	3.5	0.13
Fig. 1 & 2, t=1.82s, *r/a=0.6*	10.0	1.5	0.17
Figs. 4, 5 & 6, *r/a=0.6*	8.6	1.3	0.17

Table V. DIII-D transport anlaysis[36] shows $\chi_e < \chi_{e,GB}$ within the internal transport barrier at *r/a=0.35*, while $\chi_e < 10\chi_{e,GB}$ in the L-mode edge plasma (*r/a=0.6*).

Inside the internal transport barriers (at *r/a=0.35* in both discharges) the electron thermal conductivity is less than one electron gyro-Bohm, as one would expect from ETG turbulence near marginal stability. In the L-mode edge plasma (at *r/a=0.6* for both

discharges) the electron thermal conductivity is about 10 electron gyro-Bohms — consistent with our ETG simulation results (with kinetic ions) at high magnetic shear (the magnetic shear at $r/a=0.8$ was $s\approx 1.2$ in both of these discharges). This general pattern is repeated in both JET[37] and JT-60U.[38] Within the internal transport barrier $\chi_e/\chi_{e,GB}$ is less than or of the order of one, rising to values of less than or about 25 in the L-mode plasma outside the barrier.

ETG transport may also be important in NSTX spherical tokamak where transport analysis[40,41] shows that χ_e is often substantially larger than χ_i and has different variation with the plasma minor radius. This is the case in NSTX shot #108213 at $t=0.3s$, a neutral beam heated L-mode discharge analyzed by Stutman et al.[40] Examining the mid-radius ($0.3 \le r/a \le 0.5$) from Fig. 1a of Ref. 40 (see Table VI) we find that χ_e is less than $10\chi_{e,GB}$, consistent with our ETG simulations results. Stutman et al[40] performed a stability analysis at $r/a=0.4$ of shot #108213 at $t=0.3s$ and concluded that ETG modes are linearly unstable in this region. This general behavior ($\chi_e > \chi_I$ with different radial variation) is also seen in high-harmonic fast wave (HHFW) heated L-mode discharges (e.g., shot #106194 at $t=2.43s$)[41] and neutral beam heated H-mode discharges (e.g., shot 112581 at $t=0.55s$[40] and shot #109070 at $t=0.45s$[41]). Reviewing this data we again find $\chi_e \le 10\chi_{e,GB}$ at mid-radius, consistent with our ETG turbulence simulations.

Here we have demonstrated that there are many experiments where the observed value of $\chi_e / \chi_{e,GB}$ is in a range that could be explained by ETG turbulence. Of course this does not rule out that ITG+TEM (trapped electron mode) turbulence might be the dominant

source of electron thermal transport in most plasmas. To identify more precisely when ETG is playing a significant role in a particular experiment, it will be necessary to carry out more detailed analysis with self-consistent transport modeling, including the effects of marginal stability and equilibrium-scale sheared flows.

Table VI. NSTX transport analysis

	$\chi_e/\chi_{e,GB}$	T (keV)	L_T (m)
shot #1080213@t=0.3s, r/a=0.3	4.4	0.82	0.22
shot #1080213@t=0.3s, r/a=0.4	6.4	0.56	0.15
shot #1080213@t=0.3s, r/a=0.5	7.5	0.48	0.12
shot #112581@t=0.55s, r/a=0.7	6.0	0.46	0.10
shot #106194@t=2.43s, R=1.2m	7.4	1.02	0.33
shot #109070@t=0.45s, R=1.35m	10.4	0.80	0.26

Table VI. Transport analysis from NSTX[40,41] shows χ_e consistently less than about $10\chi_{e,GB}$ at mid-radius

VII. Summary and Conclusions

The definition and successful completion of a nonlinear benchmarking exercise is an important step in studying a new regime of plasma microturbulence. We have completed a nonlinear benchmarking of ETG turbulence between four plasma microturbulence codes (GYRO, PG3EQ, GS2, and GENE), achieving agreement in the (time and space)

averaged electron thermal transport. The turbulent intensity, correlation functions, turbulent spectra, and *rms* $E\times B$ flow shear are also in substantial agreement. Our simulation results are shown to be well-converged in time step, velocity-space resolution, parallel grid resolution, and the radial extent of the simulation flux-tube by varying these numerical parameters in the continuum (GYRO) and PIC (PG3EQ) simulation codes. Convergence with respect to resolution in the plane perpendicular to $\boldsymbol{B}$ is asymmetric. $\langle\chi_e\rangle$ is found to increase with increasing bi-normal resolution until convergence in bi-normal resolution is achieved at $k_{y,max}\rho_e > 1.4$. At fixed bi-normal resolution convergence in radial resolution is achieved as the radial resolution approaches the bi-normal resolution (for runs which are under resolved in bi-normal resolution) or $k_{x,max}\rho_e > 1.5$ (for runs which are converged in bi-normal resolution). Similarly, $\langle\chi_e\rangle$ is found to increase with increasing bi-normal flux-tube dimension. The problems of convergence in bi-normal resolution and bi-normal flux tube extent discussed in Sec. III will be addressed in future work. In this paper we have compared results between codes while holding the bi-normal resolution and flux tube extent constant. The demonstration that continuum and PIC simulations of ETG turbulence achieve a common result when addressing a common operating point should allow community discussion of ETG simulation results to move beyond questions of code accuracy to the physics underlying ETG turbulence. Three such issues addressed here are (1) the structure of the ETG spectrum, (2) the breakdown of the adiabatic ion model as the magnetic shear is increased beyond $s\approx 0.4$, and (3) the experimental relevance of the electron heat transport rate observed in simulations of ETG turbulence.

The fluctuation spectrum of ETG turbulence differs from that of ITG turbulence due to the absence of a long wavelength cutoff in the ETG fluctuation spectrum. Within the adiabatic ion (for ETG) or electron (for ITG) models the linear growth spectra of ETG and ITG are isomorphic so the absence of a long wavelength cutoff in the ETG fluctuation spectrum must reflect differences in the nonlinear physics of ETG turbulence relative to ITG turbulence. The difference in the adiabatic species response for zonal flows in ITG vs. ETG turbulence makes the coupling to zonal flows stronger for ITG turbulence. This stronger coupling is probably responsible for the long wavelength cutoff observed in the ITG turbulent spectrum. The absence of a long wavelength cutoff in the ETG turbulent spectrum leads to an increase in the electron heat-flux with the bi-normal extent of the simulation flux-tube. It is possible that a realistic magnetic geometry with good flux-surface-averaged curvature will introduce a long-wavelength cut-off through linear damping of long-wavelength ETG modes. In the absence of any long-wavelength cut-off we can expect that ETG turbulence will be manifested in experimental measurements of the electron density fluctuation spectrum as a "shoulder" at $k_\perp\rho_e \approx 0.15$ on a spectrum which otherwise decreases monotonically from the peak (associated with ion-scale turbulence) in the neighborhood of $k_\perp\rho_i \approx 0.2$. The fluctuation spectrum should exhibit a change in the direction of mode propagation from the ion diamagnetic direction at low $k_\perp$ ($k_\perp\rho_i \le 0.2$) to the electron diamagnetic direction at higher values of $k_\perp$ ($k_\perp\rho_e \approx 0.15$). It is our expectation from examining simulations of both ITG and ETG turbulence that there will only be a well-defined frequency at a given value of $k_\perp$ below the ITG spectral peak at $k_\perp\rho_i \le 0.2$ and near the ETG shoulder in the spectrum at

$k_\perp \rho_e \approx 0.15$. We anticipate that it will be difficult to associate a frequency and a direction of propagation to turbulent fluctuations at other values of $k_\perp$.

Within the adiabatic ion model, and for the parameters studied here, there is a dramatic increase in both the intensity of the ETG turbulence and the associated electron heat transport as the magnetic shear is increased beyond $s \approx 0.4$. In the high shear (and high transport) regime the ETG turbulent spectrum is dominated by the mode with $k_r = 0$ and the lowest non-zero bi-normal wavenumber allowed within the cross-section of the flux-tube simulation. While this phenomena is reminiscent of the ETG "streamers" described in the work of Jenko and Dorland,[13-15] there is an important distinction to be made. The ETG streamers described by Jenko and Dorland were microscopic in the sense that their radial extent could be measured in units of ρ_e, while the ETG streamers seen in our adiabatic ion simulations with $s \geq 0.4$ are macroscopic in the sense that their radial extent is greater than the radial width of the flux tube, going to infinity in the limit $\rho_e^* = \rho_e / a \rightarrow 0$. (Jenko and Dorland's simulations were with trapped particles turned off, which provides a long wavelength cutoff in the spectrum and helped their simulations saturate.) The appearance of macroscopic streamers in recent ETG simulations[11,12,20,21] is also likely an artifact of the adiabatic ion model often employed in simulations of ETG turbulence. The absence of such macroscopic streamers in higher-fidelity simulations of ETG turbulence (*e.g.*, simulations with kinetic ions) bodes well for experimental efforts to detect ETG turbulence employing diagnostics sensitive to fluctuations with a finite radial wavenumber.

Perhaps the most interesting result of this numerical study of ETG turbulence is the demonstration that ETG turbulence can produce an electron thermal conductivity, $\langle\chi_e\rangle$, as large as $14\ (\rho_e/L_T)\rho v_{te}$ — comparable to that obtained by in the limit $r/R_0 \rightarrow 0$ by Jenko and Dorland,[13-15] and well within the range obtained from transport analyses of tokamak experiments within thermal barriers and in the L-mode edge of many discharges.[36-38] Similar values of the electron thermal transport are also observed in transport analyses of spherical tokamaks.[40,41] This demonstration is not conclusive because the simulations in question were not converged in bi-normal resolution. However, our experience indicates that $\langle\chi_e\rangle$ increases with increasing bi-normal resolution so these values of $\langle\chi_e\rangle$ probably represent a lower limit. Recent simulations[31] have found that long wavelength ITG/TEM turbulence may reduce ETG turbulent intensities and transport levels, so that ETG is more likely to be important in regimes where the ITG/TEM modes are reduced or have a higher threshold, such as in regimes with hot ions or large equilibrium-scale sheared flows. Hence, this work supports the tentative conclusion that ETG turbulence is a candidate for explaining the electron thermal transport in some tokamak discharges.

Acknowledgements

We gratefully acknowledge Bruce Cohen for his interest, advice, and careful editing; and Stan Kaye for helpful comments regarding transport analysis on NSTX. This work was performed under the auspices of the U.S. Department of Energy by UC, Lawrence Livermore Nat. Lab. under contract No. W-7405-ENG-48, by Princeton Plasma Physics Laboratory under contract No. DE-AC02-76CH03073, by the Center for Multiscale

Plasma Dynamics at the University of Maryland and UCLA under contract No. DE-FC02-04ER54784, and at General Atomics under contract Nos. DE-FG03-95ER54309 and DE-FG02-92ER54141. The simulations described here made use of resources at the National Energy Research Supercomputer Center under Department of Energy Contract No. DE-AC03-76SF00098.

References

1. B. Coppi and G. Rewoldt, in *Advances in Plasma Physics,* edited by A. Simon and W. B. Thompson (John Wiley and Sons, New York, 1976), Vol. 6, p. 421.

2. P. N. Guzdar, C. S. Liu, J. Q. Dong, and Y. C. Lee, Phys. Rev. Lett. **57**, 2818 (1986).

3. Y. C. Lee, J. Q. Dong, P. N. Guzdar, and C. S. Liu, Phys. Fluids **30**, 1331 (1987).

4. W. Horton, B. G. Hong, and W. M. Tang, Phys. Fluids **31**, 2971 (1988).

5. R.E. Waltz, G.D. Kerbel, and J. Milovich, Phys. Plasmas **1**, 2229 (July, 1994).

6. B.I. Cohen, D.C. Barnes, J.M. Dawson, G.W. Hammett, W.W. Lee, G.D. Kerbel, J.-N. Leboeuf, P.C. Liewer, T. Tajima, and R.E. Waltz, Computer Physics Communications **87**, 1 (1995).

7. A.M. Dimits, T.J. Williams, J.A. Byers, and B.I. Cohen, Phys. Rev. Lett. **77**, 71 (July, 1996).

8. A.M. Dimits, G. Bateman, M.A. Beer, B.I. Cohen, W. Dorland, G.W. Hammett, C. Kim, J.E. Kinsey, M. Kotschenreuther, A.H. Kritz, L.L. Lao, J. Mandrekas, W.M. Nevins, S.E. Parker, A.J. Redd, D.E. Shumaker, R. Sydora, and J. Weiland, Phys. Plasmas **7**, 969 (March, 2000).

9. R.E. Waltz, J. Candy and M.N. Rosenbluth, "Gyrokinetic turbulence simulation of profile shear stabilization and broken gyroBohm scaling", Phys. Plasmas **9**, 1938 (2002).

10. B. Labit and M. Ottaviani, Phys. Plasmas **10**, 126 (2003).

11 Z. Lin, L. Chen, Y. Nishimura, H. Qu, T.S. Hahm, J.L.V. Lewandowski, G. Rewoldt, W.X. Wang, P.H. Diamond, C. Holland, F. Zonca, and Y. Li, *Electron Thermal transport in Tokamaks: ETG or TEM Turbulence?* Fusion Energy 2004, Proc. 20th Fusion Energy Conference, Vilamoura, 2004 (IAEA, Vienna, 2005) paper TH8_4. See and http://www-naweb.iaea.org/napc/physics/fec/fec2004/datasets/index.html .

12. Z. Lin, *On Structures in Electron Temperature Gradient Turbulence*, Bull. Am. Phys. Soc. (November, 2004). See http://www.aps.org/meet/DPP04/baps/index.html.

13. F. Jenko, W. Dorland, M. Kotschenreuther, and B.N. Rogers, Phys. Plasmas **7**, 1904 (May, 2000).

14. W. Dorland, F. Jenko, M. Kotschenreuther, and B.N. Rogers, PRL **85**, 5570 (December, 2000).

15. F. Jenko and W. Dorland, PRL **89**, 225001 (November, 2002).

16. Y. Idomura S. Tokuda, and Y. Kishimoto, 2004 *Fusion Energy 2004: Proc. 20th Int. Conf. (Vilamoura, 2004)* (Vienna: IAEA) CD-ROM file TH/8-1 and http://www-naweb.iaea.org/napc/physics/fec/fec2004/datasets/index.html

17. Y. Idomura, S. Tokuda, and Y. Kishimoto, Nuclear Fusion **45**, 1571 (2005).

18. J. Li and Y. Kishimoto, Phys. Plasmas **11**, 1493 (April, 2004).

19. J.Q. Li, Y. Kishimoto, N. Miyato, T. Matsumoto, and J.Q. Dong, Nuclear Fusion **45**, 1293 (2005).

20. Z. Lin, L. Chen, and F. Zonca, Phys. Plasmas **12**, 056125 (May, 2005).

21. W.M. Nevins, G.W. Hammett, A.M. Dimits, W. Dorland, and D.E. Shumaker, Phys. Plasmas **12**, 122305 (December, 2005).

22. W.L. Kruer, Report of the June 2005 PSACI PAC meeting (private communication).

23. J. Candy and R.E. Waltz, "An Eulerian gyrokinetic-Maxwell solver", J. Comput. Phys. **186**, 545 (2003).

24. T.S. Hahm, P.H. Diamond, Z. Lin, and S.-I. Itoh, Plasma Phys. Control. Fusion **46**, A323 (2004).

25. Z. Lin, S. Ethier, T.S. Hahm, and W.M. Tang, Phys. Rev. Lett. **88**, 195004 (May, 2002).

26. J. Candy, R.E. Waltz and W. Dorland, "The local limit of global gyrokinetic simulations", Phys. Plasmas **11**, L25 (May, 2004).

27. M.N. Rosenbluth and F.L. Hinton, Phys. Rev. Lett. **80**, 724 (1998).

28. P.H. Diamond, S.-I. Itoh, K. Itoh, T.S. Hahm, Plasma Physics and Controlled Fusion **47** (5), R35-R161 (2005).

29. Y. Xiao and P.J. Catto, "Short wavelength effect on the collisionless neoclassical polarization and residual zonal flow level", submitted to Phys. Plasmas (July, 2006).

30. J. Candy, “Coupled ITG/TEM-ETG Gyrokinetic Simulations”, Proceedings of the 21st IAEA Fusion Energy Conference (16 - 21 October, Chengdu, China) (Vienna: IAEA) paper TH2-1, see http://www-pub.iaea.org/MTCD/Meetings; R.E. Waltz, J. Candy, and M. Fahey, "Coupled ITG/TEM-ETG gyrokinetic simulations" to be submitted to Phys. Plasma APS edition,

31. S. Parker, Bull. Am. Phys. Soc. (November, 2005).

32. F. Jenko and A. Kendl, Physics of Plasmas **9**, 4103 (2002).

33. H. Biglari, P.H. Diamond, and P.W. Terry, Phys. Fluids B **2**, 1 (1990).

34. K.H. Burrell, Phys. Plasmas **4**, 1499 (1997).

35. T.S. Hahm, M.A. Beer, Z. Lin, G.W. Hammett, W.W. Lee, and W.M. Tang, Phys. Plasmas **6**, 922 (March, 1999).

36. B.W. Stallard, C.M. Greenfield, G.M. Staebler, C.L. Rettig, M.S. Chu, M.E. Austin, D.R. Baker, L.R. Bayor, K.H. Burrell, J.C. DeBoo, J.S. DeGrassie, E.J. Doyle, J. Lohr, G.R. McKee, R.L. Miller, W.A> Peebles, C.C. Petty, R.I. Pinsker, B.W. Rice, T.L. Rhodes, R.E. Waltz, L. Zeng, and the DIII-D Team, Phys. Plasmas **6**, 1978 (1999).

37. V.V. Parail, Yu. F. Baranov, C.D. Challis, G.A. Cottrell, B. Fischer, C. Gormezano, G.T.A. Huysmans, X. Litaudon, A.C.C. Sips, F.X. Söldner, E.M. Springmann, A. Taroni, and D.J. Ward, Nuclear Fusion **39**, 429 (1999).

38. H. Shirai, M. Kikuchi, T. Takizuka, T. Fujita, Y. Koide, G. Rewoldt, D. Mikkelsen, R. Budny, W.M. Tang, Y. Kishimoto, Y. Kamada, T. Oikawa, O. Naito, T. Fukuda, N. Isei, Y. Kawano, M. Azumi, and the JT-60 Team, Nuclear Fusion **39**, 1713 (1999).

39. C.C. Petty, M.R. Wade, J.E. Kinsey, D.R. Baker, and T.C. Luce, *Phys. Plasmas* **9**, 128 (January, 2002).

40. D. Stutman, K.W. Hill, M.S. Kaye, M.H. Redi, E.J. Synakowski, M.G. Bell, R.E. Bell, C. Bourdelle, W. Dorland, M. Finkenthal, S. Kubota, B.P. LeBlanc, F. Levington, J.E. Menard, D.R. Mikkelsen, K. Tritz, and the NSTX Team, "Studies of Improved Electron Confinement on NSTX", Proceedings of the 20th IAEA Fusion Energy Conference (1 - 6 November 2004, Vilamoura, Portugal) (Vienna: IAEA) paper EX/P2-8, see http://www-pub.iaea.org/MTCD/Meetings .

41. B.P. LeBlanc, R.E. Bell, S.M. Kaye, D. Stutman, M.G. Bell, M.L. Bitter, C. Bourdelle, D.A. Gates, R. Maingi, S.S. Medley, J.E. Menard, D. Mueller, S.F. Paul, A.L. Roquemore, A. Rosenberg, S.A. Sabbagh, V.A. Soukhanovskii, E.J. Synakowski, J.R. Wilson, and the NSTX Research Team, Nuclear Fusion **44**, 513 (2004).

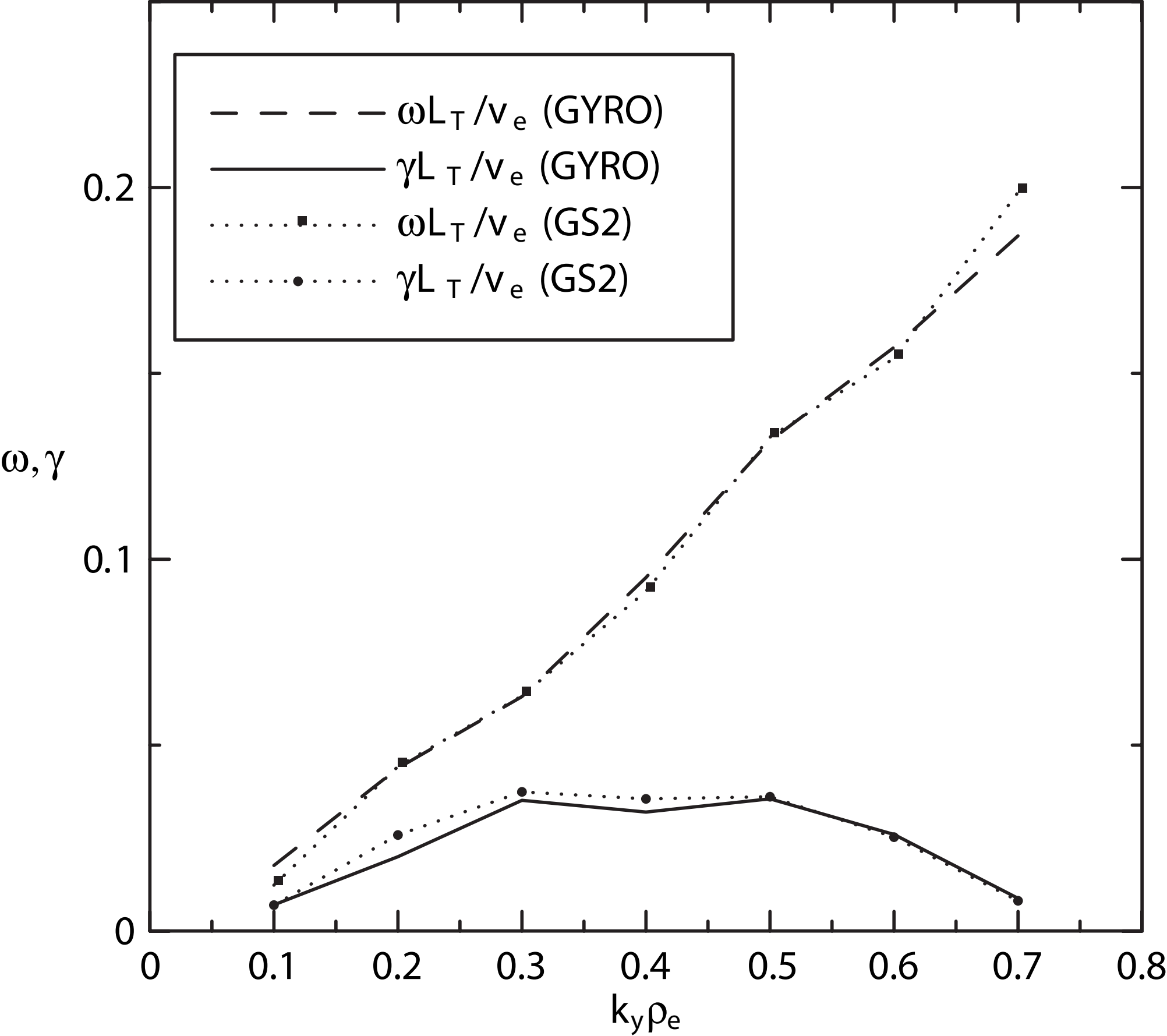
ωL_T/v_e (GYRO)
γL_T/v_e (GYRO)
ωL_T/v_e (GS2)
γL_T/v_e (GS2)
0.2
0.1
0
ω, γ
0
0.1
0.2
0.3
0.4
0.5
0.6
0.7
0.8
k_y ρ_e

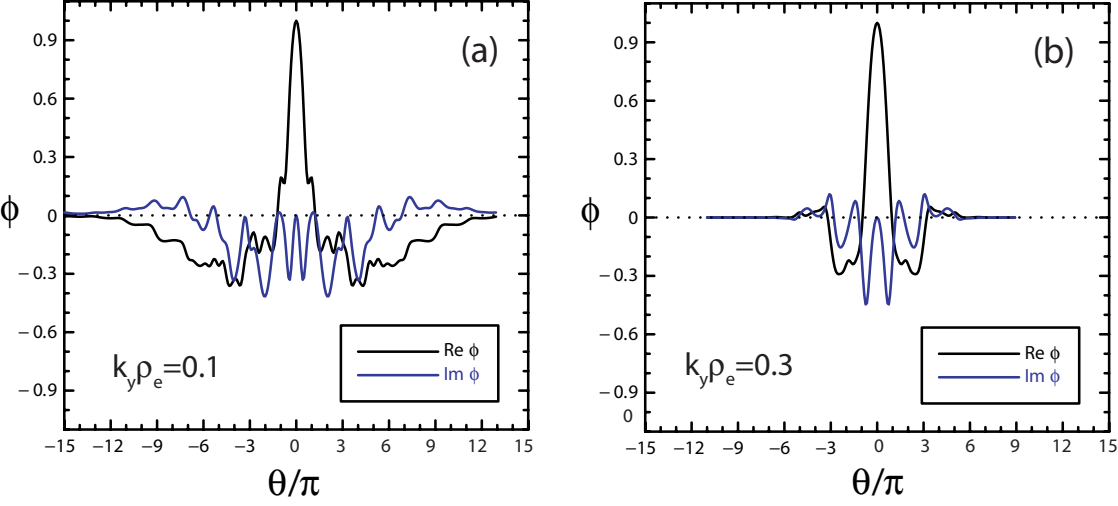
(a)
(b)
ϕ
θ/π
Re ϕ
Im ϕ
$k_y\rho_e$=0.1
$k_y\rho_e$=0.3
0.9
0.6
0.3
0
−0.3
−0.6
−0.9
−15
−12
−9
−6
−3
0
3
6
9
12
15

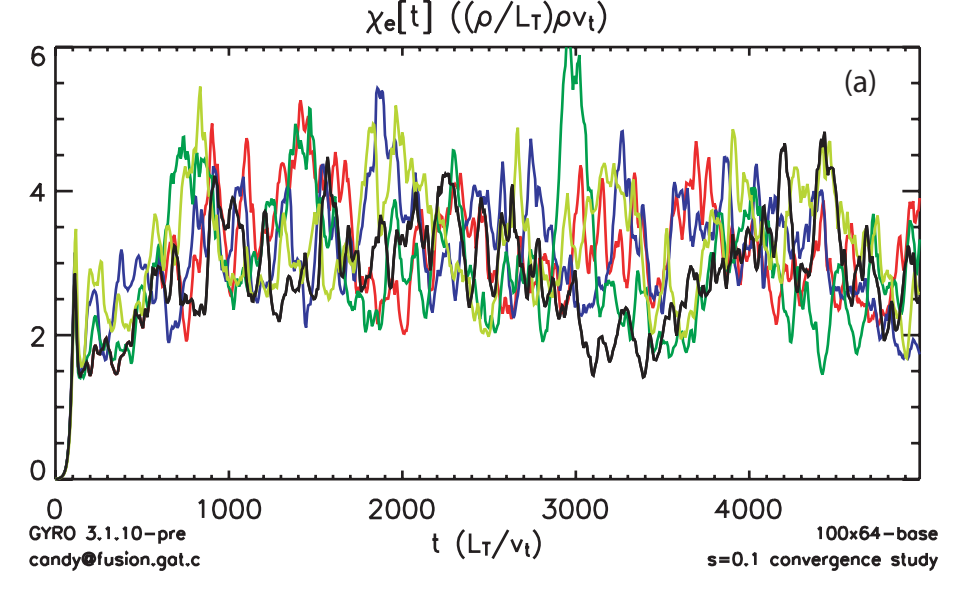
χe[t] ((ρ/LT)ρvt)
(a)
6
4
2
0
0
1000
2000
3000
4000
t (LT/vt)
GYRO 3.1.10-pre
candy@fusion.gat.c
100x64-base
s=0.1 convergence study

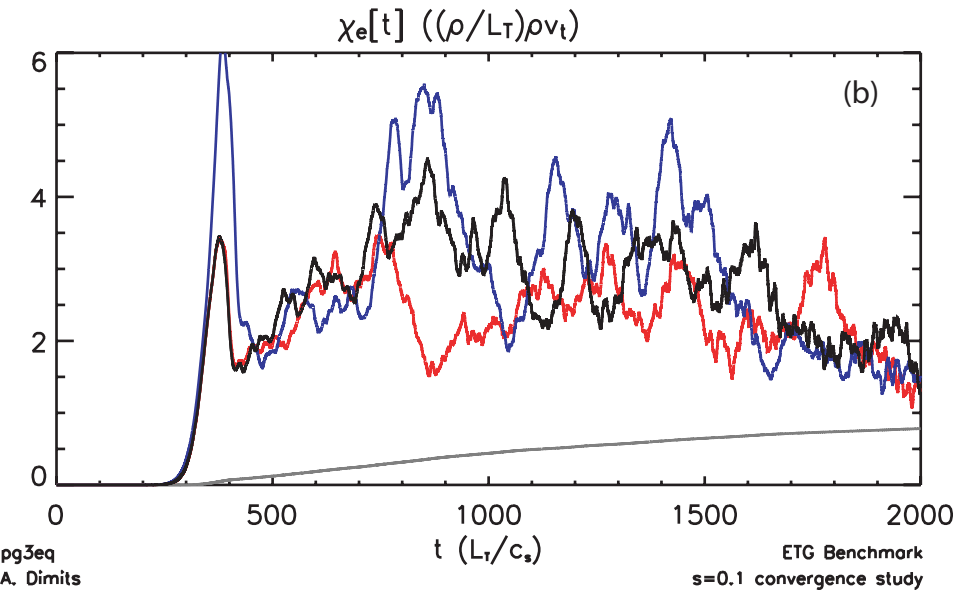
χe[t] ((ρ/LT)ρvt)
(b)
6
4
2
0
0
500
1000
1500
2000
t (LT/cs)
pg3eq
A. Dimits
ETG Benchmark
s=0.1 convergence study

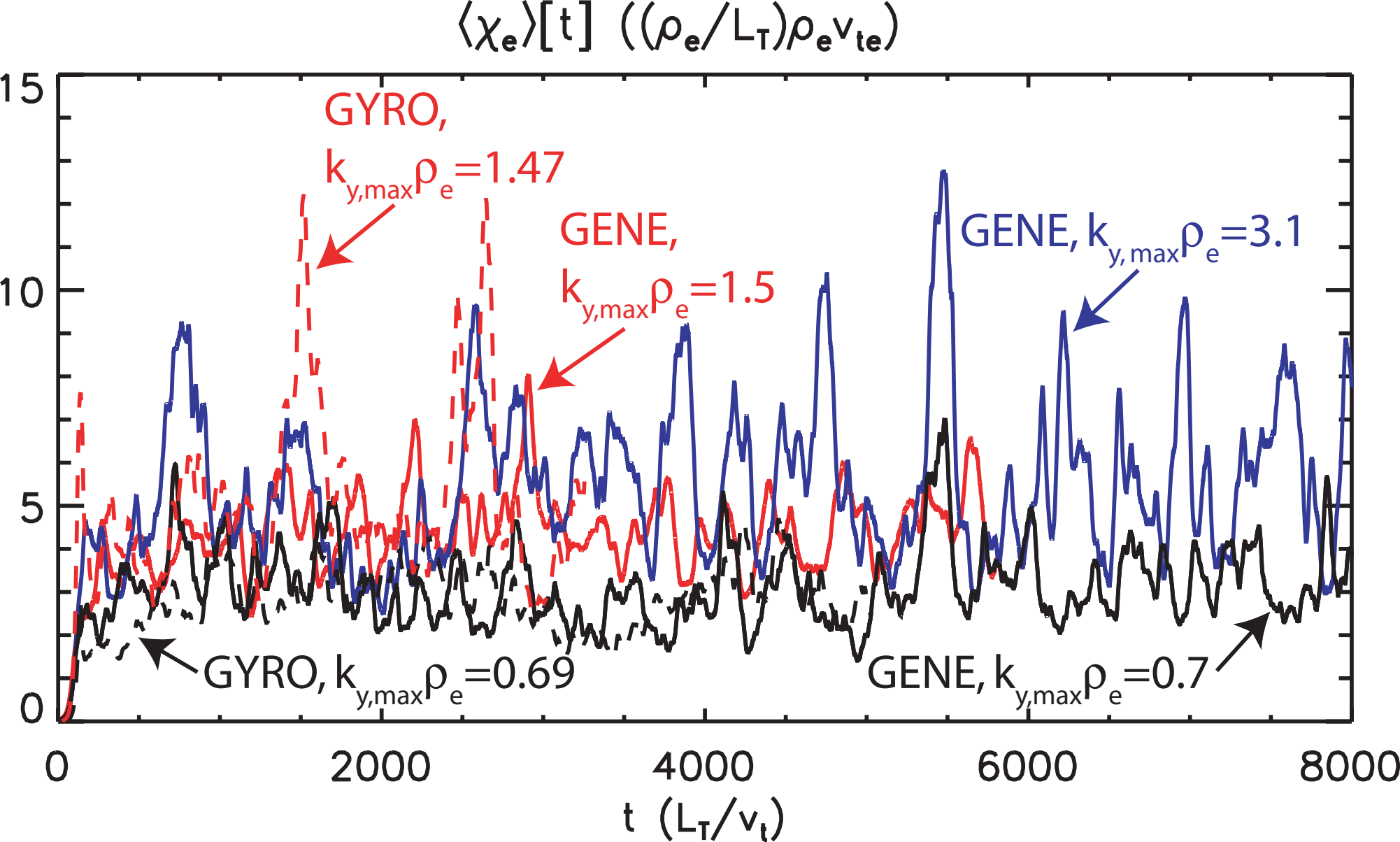
⟨χe⟩[t] ((ρe/LT)ρevte)
15
10
5
0
0
2000
4000
6000
8000
t (LT/vt)
GYRO, ky,maxρe=1.47
GENE, ky,maxρe=1.5
GENE, ky,maxρe=3.1
GYRO, ky,maxρe=0.69
GENE, ky,maxρe=0.7

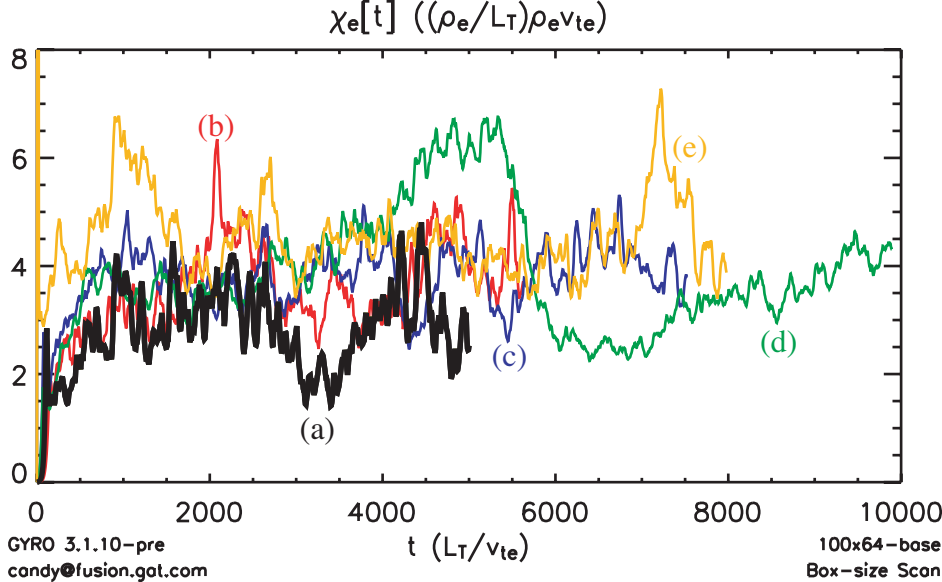
χe[t] ((ρe/LT)ρevte)
8
6
4
2
0
0
2000
4000
6000
8000
10000
(a)
(b)
(c)
(d)
(e)
t (LT/vte)
GYRO 3.1.10-pre
candy@fusion.gat.com
100x64-base
Box-size Scan

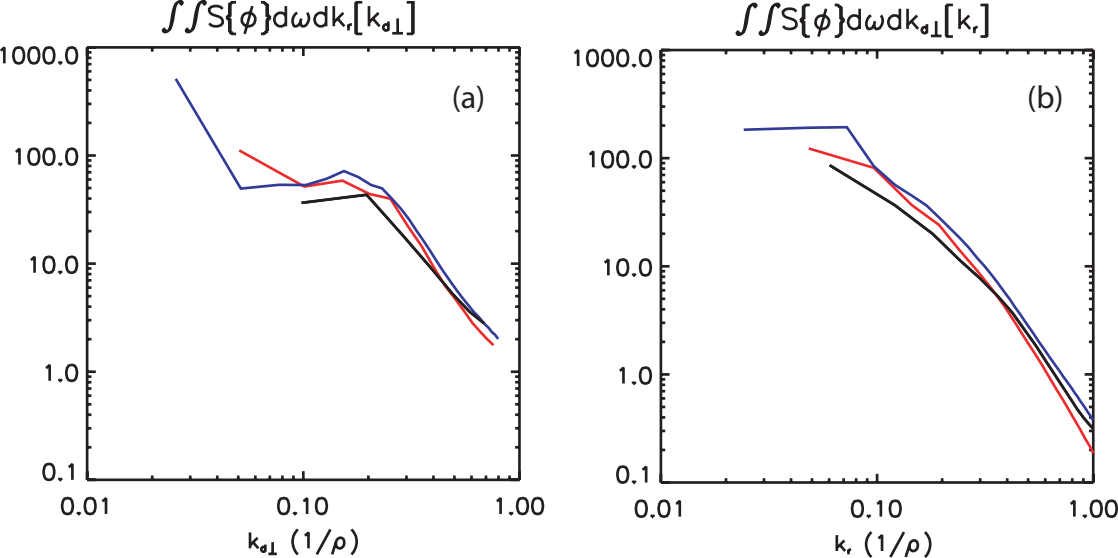
∫∫S{ϕ}dωdk_r[k_⊥]
(a)
1000.0
100.0
10.0
1.0
0.1
0.01
0.10
1.00
k_⊥ (1/ρ)
∫∫S{ϕ}dωdk_⊥[k_r]
(b)
1000.0
100.0
10.0
1.0
0.1
0.01
0.10
1.00
k_r (1/ρ)

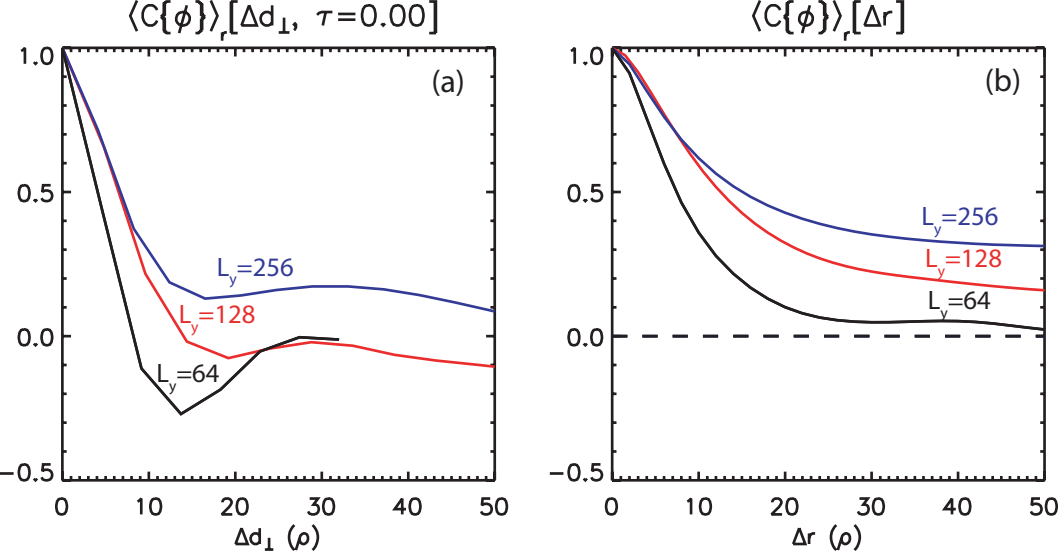
⟨C{φ}⟩r[Δd⊥, τ=0.00]
(a)
1.0
0.5
0.0
−0.5
Ly=256
Ly=128
Ly=64
0
10
20
30
40
50
Δd⊥ (ρ)
⟨C{φ}⟩r[Δr]
(b)
1.0
0.5
0.0
−0.5
Ly=256
Ly=128
Ly=64
0
10
20
30
40
50
Δr (ρ)

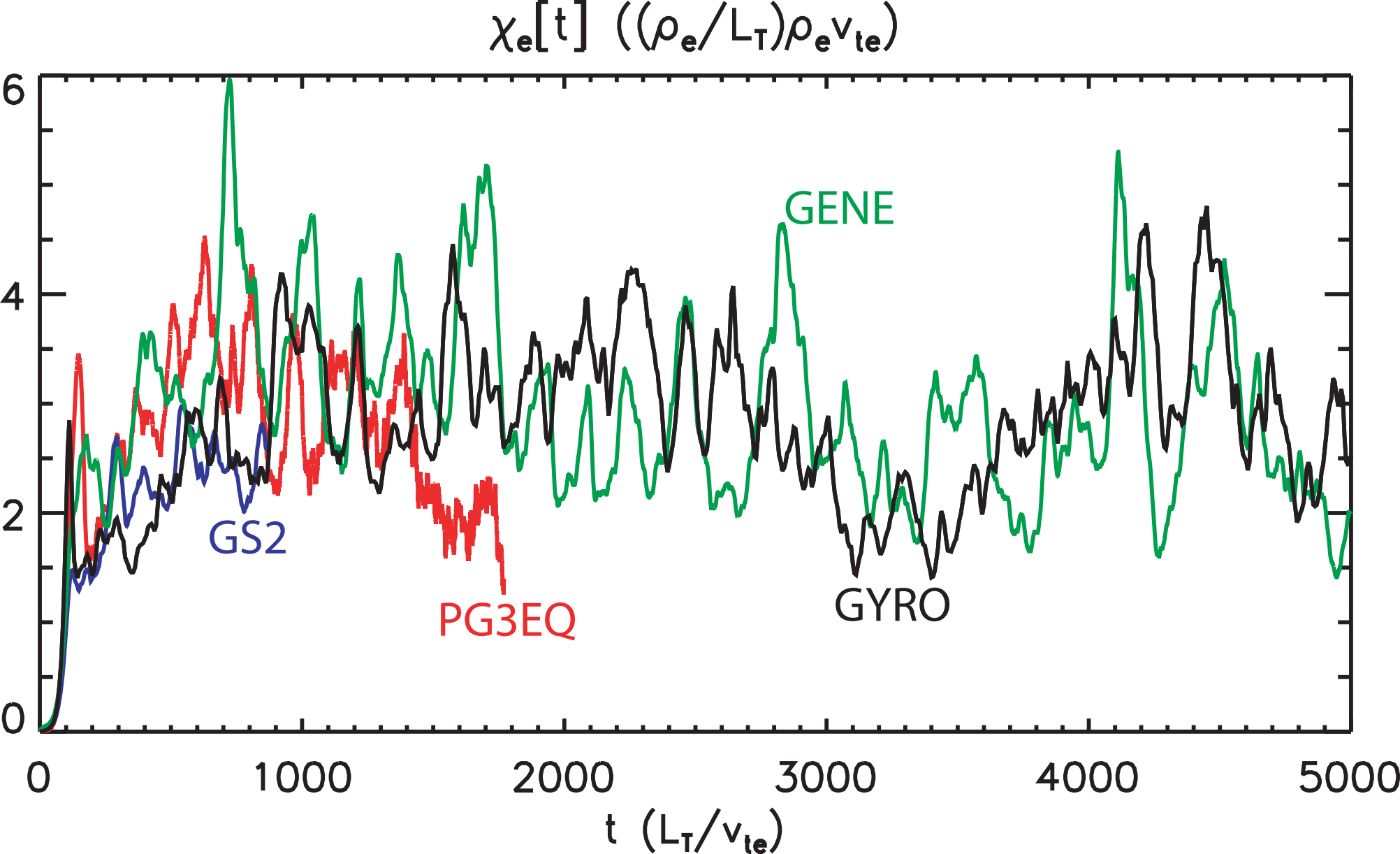
$\chi_e[t]$ $((\rho_e/L_T)\rho_e v_{te})$
6
4
2
0
0
1000
2000
3000
4000
5000
t (L_T/v_{te})
GENE
GS2
PG3EQ
GYRO

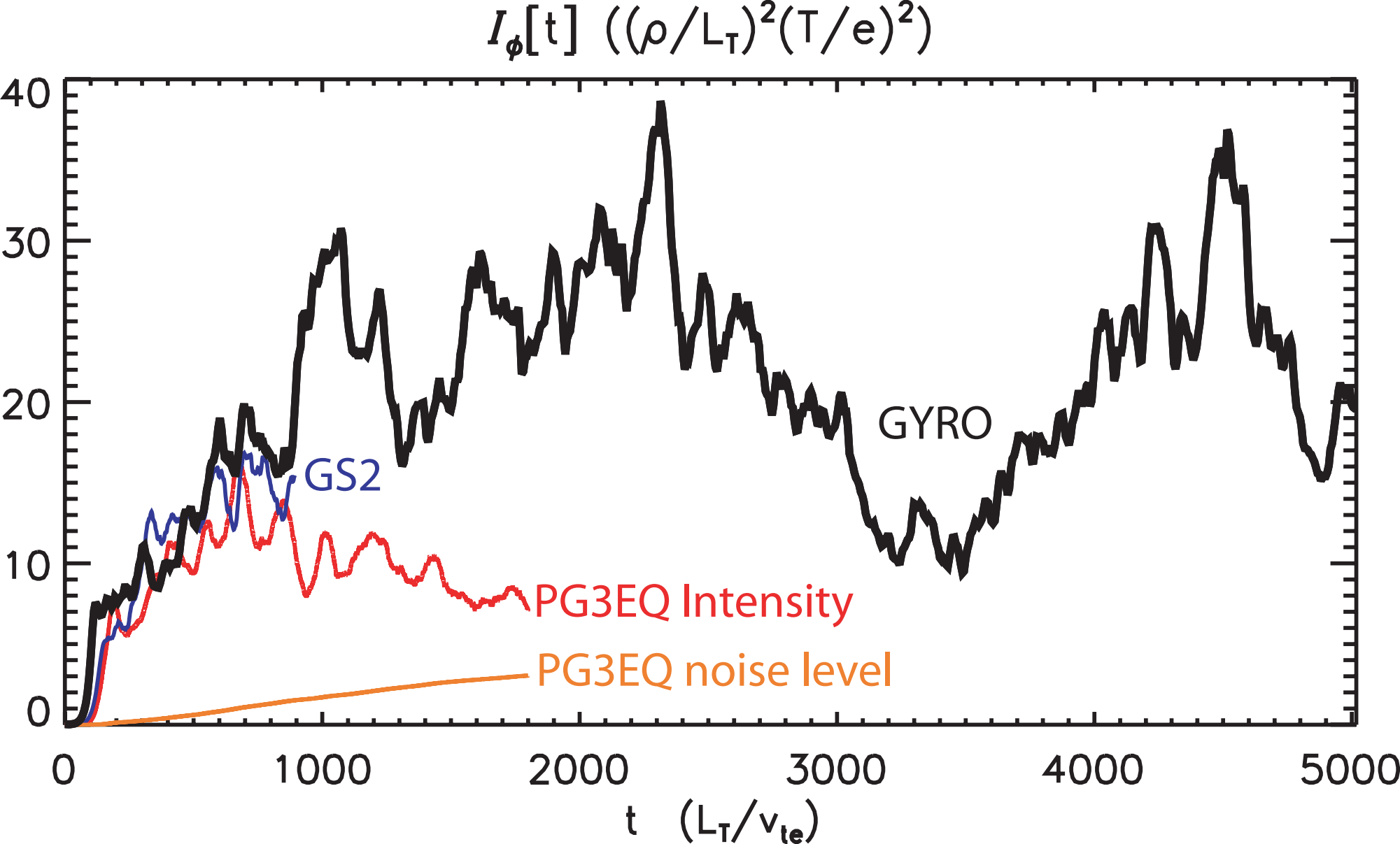
$I_\phi[t]$ $((\rho/L_T)^2(T/e)^2)$
40
30
20
10
0
0
1000
2000
3000
4000
5000
t (L_T/v_{te})
GYRO
GS2
PG3EQ Intensity
PG3EQ noise level

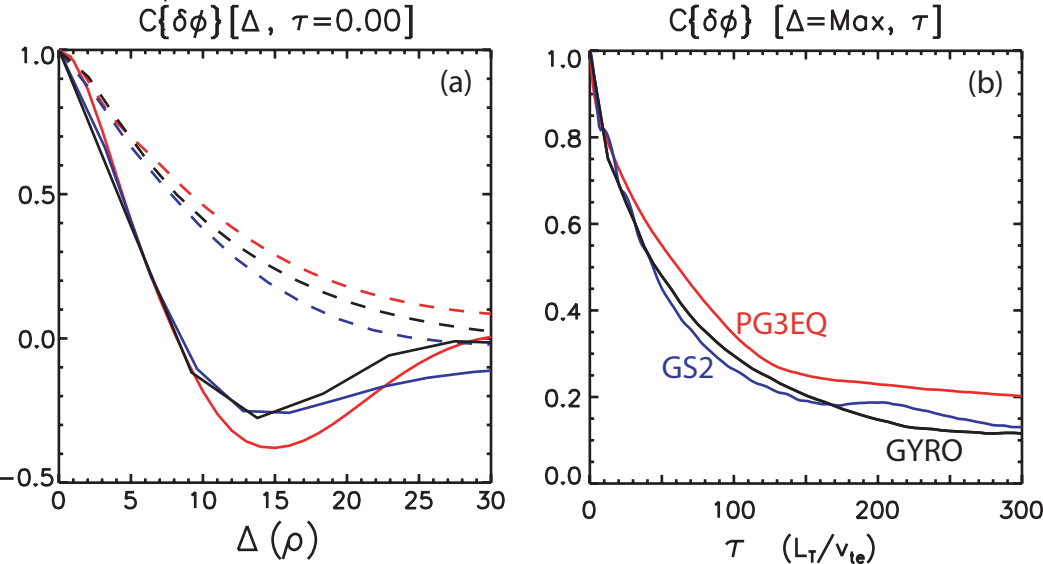
C{δφ}[Δ, τ=0.00]
(a)
1.0
0.5
0.0
−0.5
0
5
10
15
20
25
30
Δ (ρ)
C{δφ} [Δ=Max, τ]
(b)
1.0
0.8
0.6
0.4
0.2
0.0
PG3EQ
GS2
GYRO
0
100
200
300
τ (L_T/v_te)

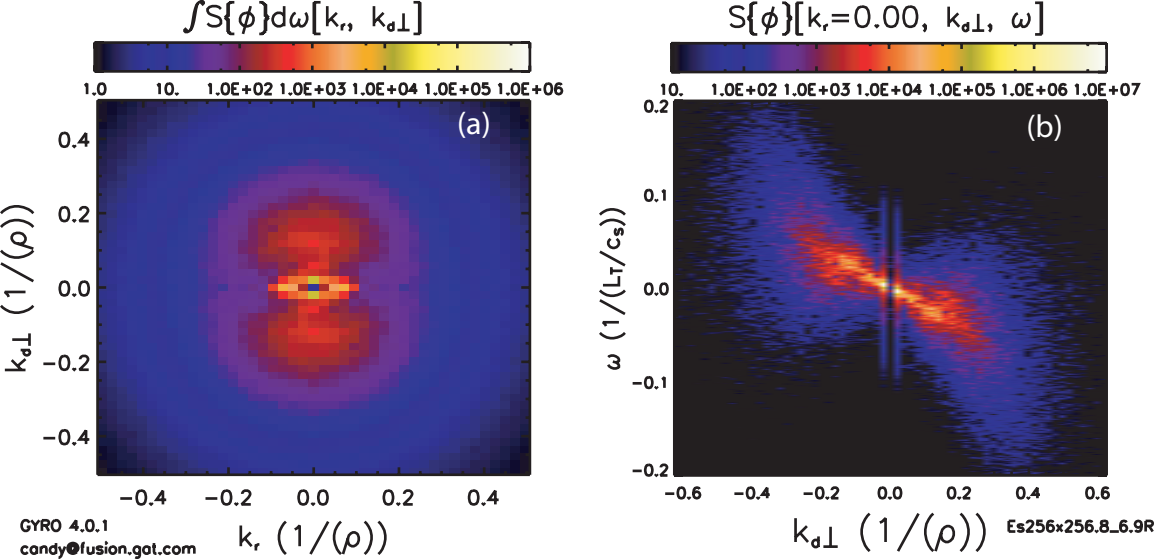
∫S{φ}dω[k_r, k_θ⊥]
1.0 10. 1.0E+02 1.0E+03 1.0E+04 1.0E+05 1.0E+06
(a)
0.4
0.2
0.0
−0.2
−0.4
k_θ⊥ (1/(ρ))
−0.4 −0.2 0.0 0.2 0.4
k_r (1/(ρ))
GYRO 4.0.1
candy@fusion.gat.com
S{φ}[k_r=0.00, k_θ⊥, ω]
10. 1.0E+02 1.0E+03 1.0E+04 1.0E+05 1.0E+06 1.0E+07
(b)
0.2
0.1
0.0
−0.1
−0.2
ω (1/(L_T/c_s))
−0.6 −0.4 −0.2 0.0 0.2 0.4 0.6
k_θ⊥ (1/(ρ))
Es256x256.8_6.9R

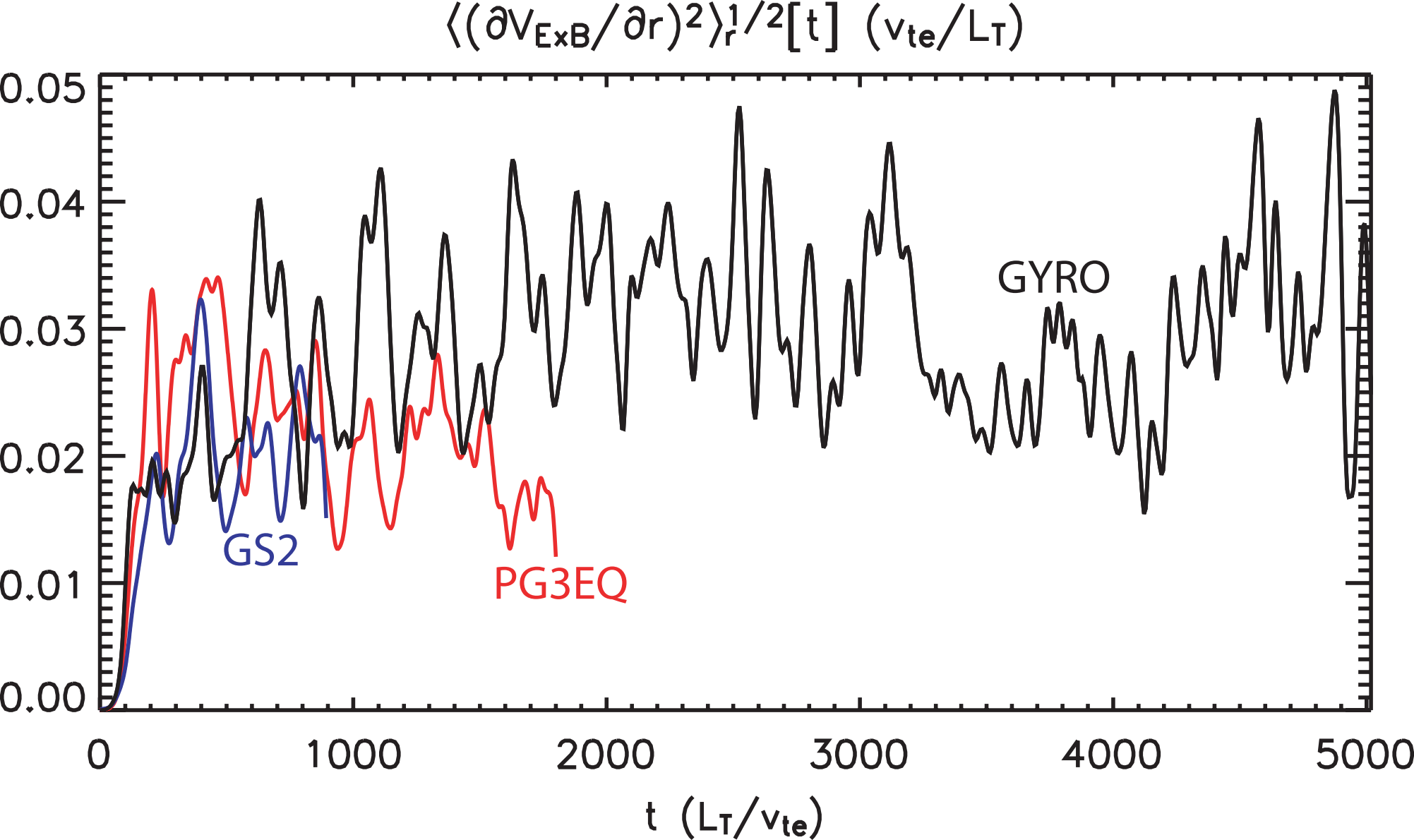
⟨(∂V_ExB/∂r)²⟩_r^1/2[t] (v_te/L_T)
0.05
0.04
0.03
0.02
0.01
0.00
0
1000
2000
3000
4000
5000
t (L_T/v_te)
GYRO
GS2
PG3EQ

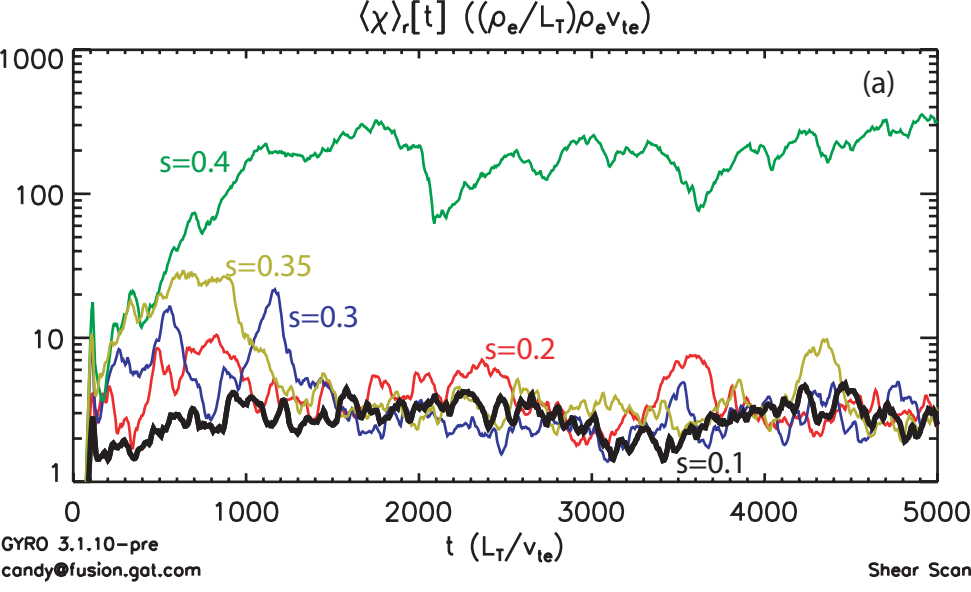
⟨χ⟩r[t] ((ρe/LT)ρevte)
(a)
s=0.4
s=0.35
s=0.3
s=0.2
s=0.1
1000
100
10
1
0
1000
2000
3000
4000
5000
t (LT/vte)
GYRO 3.1.10-pre
candy@fusion.gat.com
Shear Scan

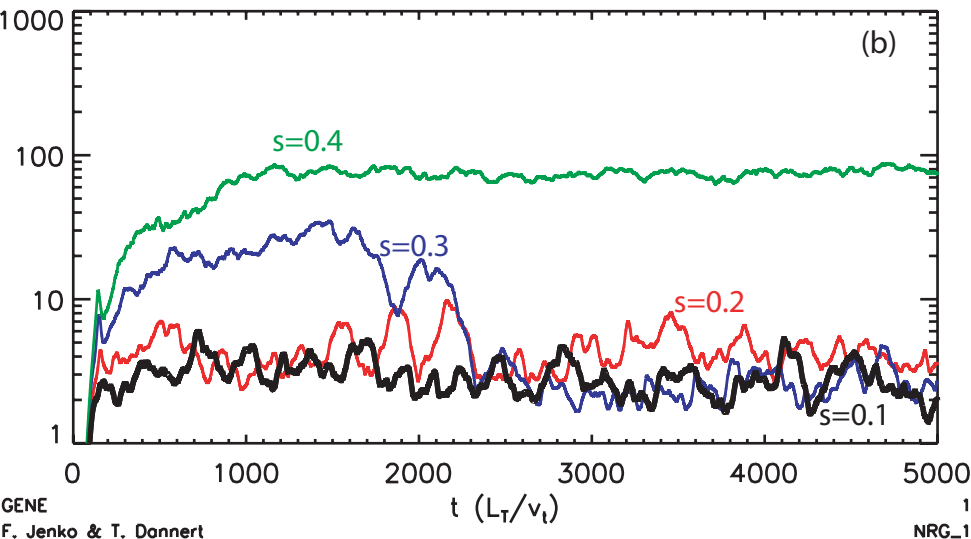
⟨χ⟩r[species=1, t] ((ρe/LT)ρevte)
(b)
s=0.4
s=0.3
s=0.2
s=0.1
1000
100
10
1
0
1000
2000
3000
4000
5000
t (LT/vt)
GENE
F. Jenko & T. Dannert
1
NRG_1

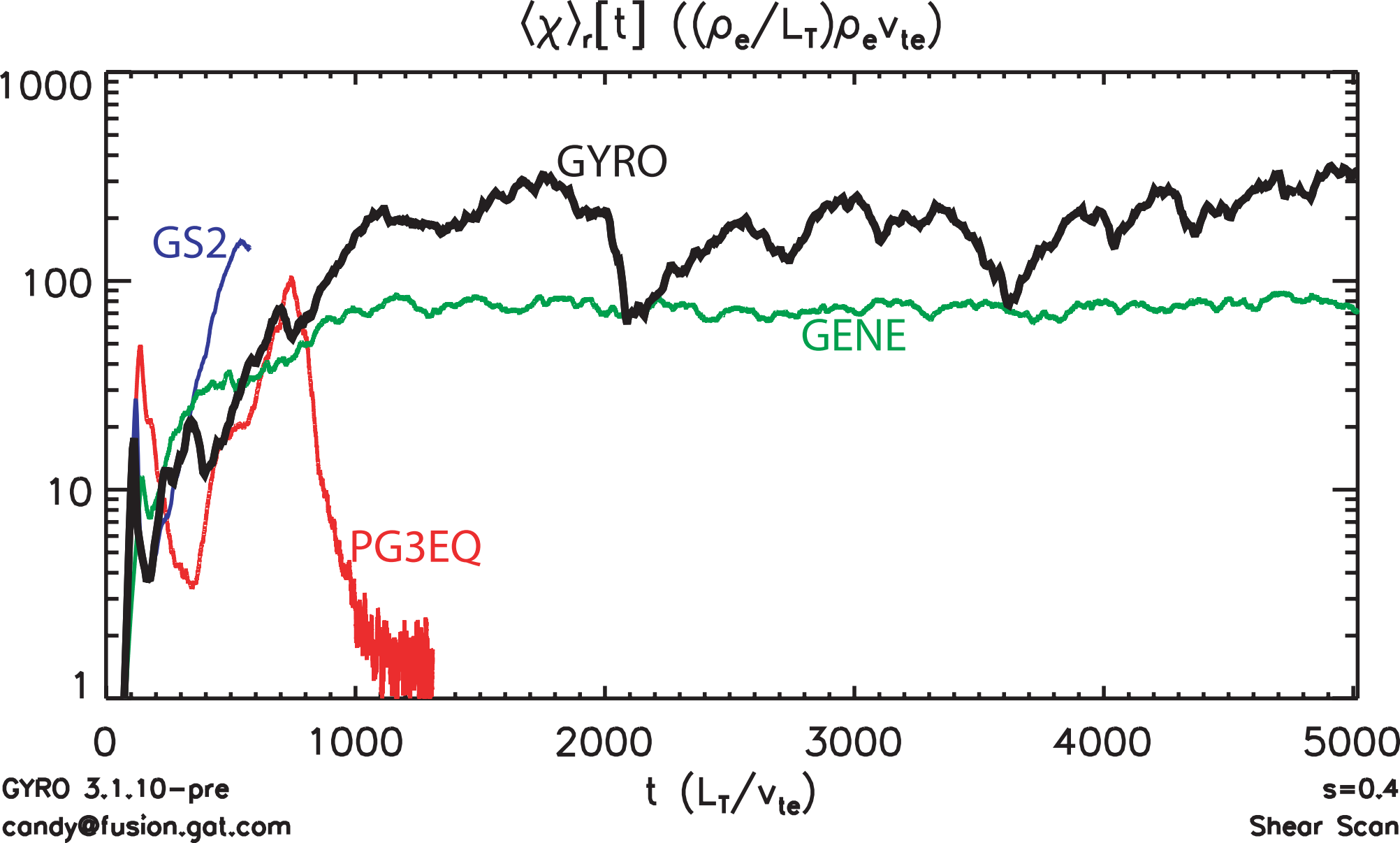
⟨χ⟩r[t] ((ρe/LT)ρevte)
1000
100
10
1
GYRO
GS2
GENE
PG3EQ
0
1000
2000
3000
4000
5000
t (LT/vte)
GYRO 3.1.10-pre
candy@fusion.gat.com
s=0.4
Shear Scan

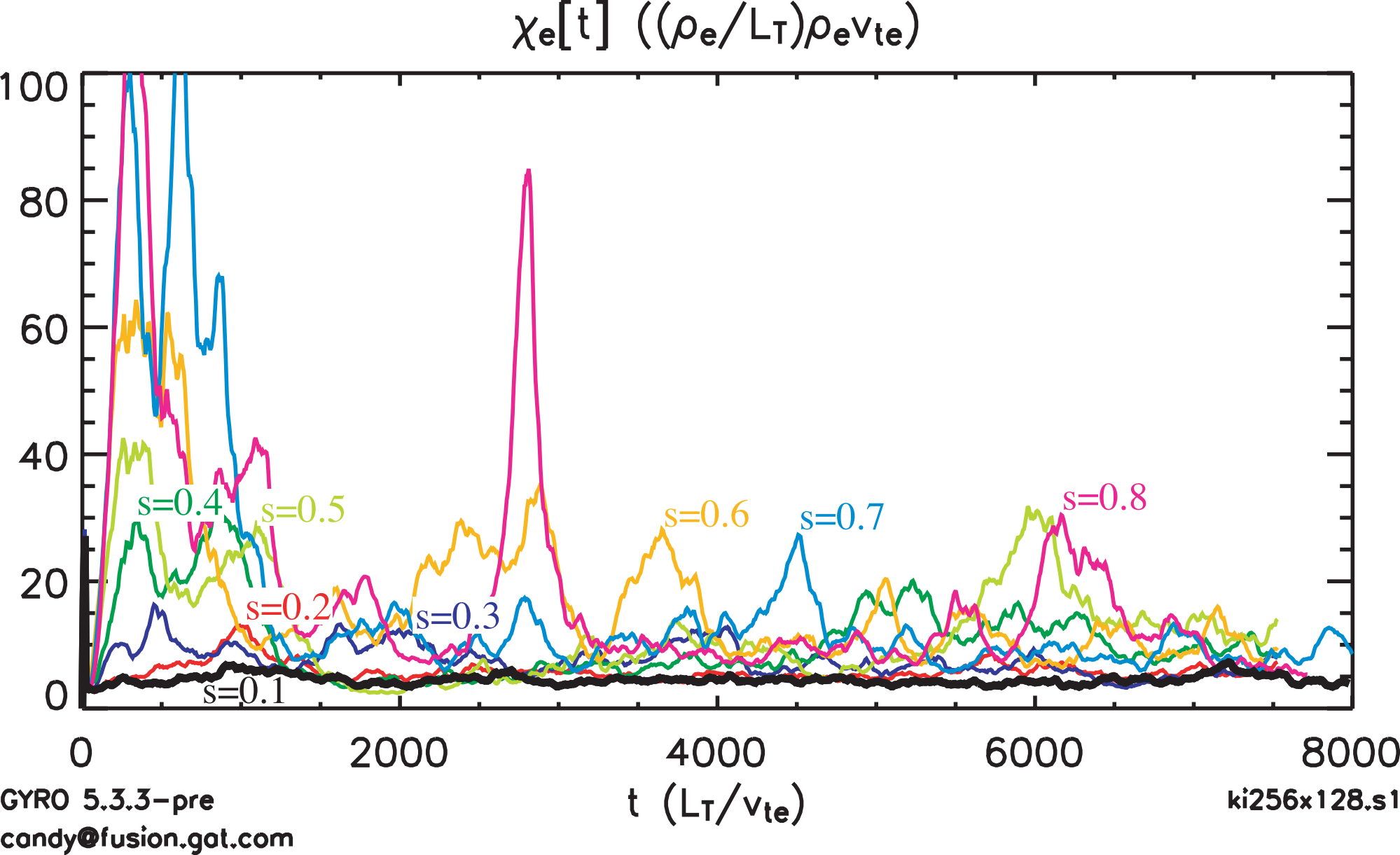
χe[t] ((ρe/LT)ρevte)
100
80
60
40
20
0
0
2000
4000
6000
8000
s=0.4
s=0.5
s=0.2
s=0.3
s=0.1
s=0.6
s=0.7
s=0.8
t (LT/vte)
GYRO 5.3.3-pre
candy@fusion.gat.com
ki256x128.s1